Human Retinotopic Mapping Using fMRI

Nicolas Wotawa, Bertrand Thirion, Eric Castet, Jean-Luc Anton, Olivier Faugeras

INRIA

INSTITUT NATIONAL DE RECHERCHE EN INFORMATIQUE ET EN AUTOMATIQUE

Human Retinotopic Mapping Using fMRI

Nicolas WOTAWA — Bertrand THIRION — Eric CASTET — Jean-Luc ANTON — Olivier FAUGERAS

N° 5472

January 2005

Thème BIO

ISSN 0249-6399 ISRN INRIA/RR--5472--FR+ENG

INRIA
SOPHIA ANTIPOLIS

Human Retinotopic Mapping Using fMRI

Nicolas WOTAWA [*] , Bertrand THIRION [†] , Eric CASTET [‡] , Jean-Luc ANTON [§] , Olivier FAUGERAS [¶]

Thème BIO — Systèmes biologiques
Projets Odyssée

Rapport de recherche n° 5472 — January 2005 — 65 pages

Abstract: We present in this report a new method for the retinotopic mapping of the human visual cortex using fMRI. This fast method allows to delineate any human's occipital retinotopic visual areas after 30 minutes in an MR scanner. Based on the known retinotopic properties of the visual cortex and on the procedures described in the literature, we first detail the experimental protocol we used. We then present the functional data analysis we perform to get the retinotopic angular maps. The algorithm to get a model of the cortical surface from the anatomical MR image is also rapidly presented. We then show the retinotopic maps projected on the latter model and compare them with the literature. Lastly, we present the choices we made to delineate these areas and extract regions of interest that can be used for further studying the human visual cortical system.

Key-words: fMRI, visual areas, retinotopy, mapping, human

[*] Nicolas.Wotawa@sophia.inria.fr
[†] Bertrand.Thirion@sophia.inria.fr
[‡] LNF, CNRS, Marseille. castet@lnf.cnrs-mrs.fr
[§] Centre IRMf, Hopital La Timone, Marseille. jl.anton@medecine.univ-mrs.fr
[¶] Olivier.Faugeras@sophia.inria.fr

Unité de recherche INRIA Sophia Antipolis
2004, route des Lucioles, BP 93, 06902 Sophia Antipolis Cedex (France)
Téléphone : +33 4 92 38 77 77 —Télécopie : +33 4 92 38 77 65

Rétinotopie par IRMf chez l'homme

Résumé : Nous présentons dans ce rapport notre méthode d'obtention et nos resultats de cartographie rétinotopique du cortex visuel humain par IRMf. Cette méthode rapide permet de délinéer les aires visuelles rétinotopiques occipitales de tout sujet humain après 30 minutes dans un scanner d'IRMf. En se fondant sur les propriétés rétinotopiques connues du cortex visuel ainsi que sur les techniques présentées dans la littérature, nous détaillons le protocole expérimental utilisé. Nous présentons ensuite l'analyse des données fonctionnelles effectuées pour obtenir les cartes rétinotopiques. Nous décrivons rapidement l'algorithme d'extraction d'un modèle cortical à partir de l'image IRM anatomique. Nous exposons les cartes rétinotopiques projetées sur ce modèle cortical et les comparons à la littérature. Enfin sont présentés les choix que nous avons effectués pour délimiter ces aires et en extraire des régions d'intérêt utilisables pour toute étude plus précises du système visuel cortical humain.

Mots-clés : IRMf, aires visuelles, retinotopie, humain

1 Introduction

Some estimates put the portion of the cortex involved in vision processings around 50% in the macaque monkey. The monkey visual cortical surface can be parcellized into more than 30 distincts areas, according to different criteria: (1) the architecture of the cortical surface (myelinisation, number of layers,...), (2) the connectivity patterns, (3) the functional characterisation and (4) the mapping of the visual field. In human studies, only the latter two are commonly used, as the first two are still invasive or too coarse (even if new imaging improvements such as high quality anatomical MRI and DT-MRI make them more and more efficient). We are interested here in labelling some areas using criterion (4), i.e. the retinotopic representation of the visual field on the cortical surface. With such a criterion, the first "low level" areas were first revealed using fMRI in 1994, starting with the pioneering study of Engel *et al.* [7] and followed by many others since [17, 4, 23, 30].

Despite this quite abundant literature on the subject, bringing under control the complete chain of processing from the experimental part to the segmentation of the retinotopic areas found on the cortical surface is not straightforward.
We describe in this report the choices we made and compare some aspects of our method and our results with those published in the litterature.

2 Principles of Vision and Retinotopy

In this section, we briefly describe the primate visual system and the organization of the visual cortex. For more precise descriptions, see [15, 1, 11].

2.1 The visual system

In primates (in particular in humans), the visual system includes many anatomical elements, from the eye to the cortex.
The human eye is approximately 2.5 cm long and weighs 7 grams. Six bands of muscles allow the control of its displacements to probe the environment. Light goes successively through the cornea, the aqueous humor, and the pupil, whose size is controlled by a muscle, the iris (giving the eye its external color). Next it passes through the lens, whose shape is controlled by the ciliary muscles, before entering the vitreous humor. It finally strikes the retina, which is covered with over 125 million photosensitive receptors of two families: the cones (around 8 millions, mainly concentrated in the center of the retina, the fovea) are responsible for chromatic and normal lighting condition vision (called *photopic*), and the rods (around 120 millions, found everywhere except in the fovea), dealing with black and white perception and low-lighting conditions (called *scotopic*). These receptors translate lighting information into electrical information, transmitted to the optical nerves via the ganglion cells. The two optical nerves cross, forming the optic chiasm, after which information is transmitted by visual hemifield (separated vertically with respect to the head position): the information from photons striking the left parts of both retina and corresponding to the right visual field is brought together to form the left optical tractus (see figure 1).

The vast majority of the optical tracts fibers gets projected to a part of the thalamic sensory relay system, the Lateral Geniculate Nucleus (LGN), whose axons finish in the primary visual cortex. The cortex is roughly a sheet of tissue (mainly the neurons soma) that makes up the outer layer of the brain. The thickness of the cerebral cortex varies from 2.5 to 6 mm. Neuroanatomists have observed that the cortical neurons appear to be organized in various layers (usually six) tangentially to the surface and also in columns. Globally, the cortex is made of various areas differentiated histologically as well as functionally. It is in particular the case for the visual cortical system, whose first areas are located at the occipital lobe, i.e. at the back of the skull. Various visual areas have already been identified in humans; we can cite V1 (for Primary visual area), V2 (subdivided in two parts, V2v for *ventral* and V2d for *dorsal*, V3, VP (Ventral Posterior area), V3A (V3 *Accessory*), V4v, V5,...An important property of most of these areas is their retinotopic organization, which allows us to differentiate them as we will see below.

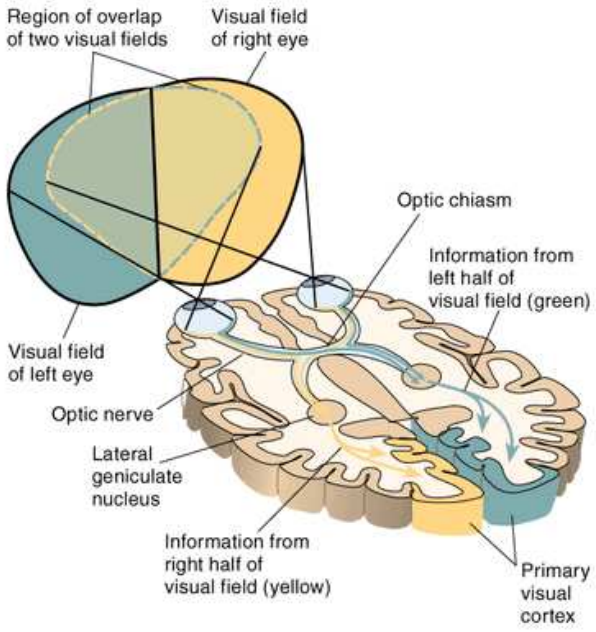

Figure 1: The path of the visual information from the eyes to the primary visual cortex. From *http://homepage.psy.utexas.edu/homepage/Class/Psy308/Salinas/Vision/Vision.html*

2.2 The cortical retinotopic organization

The general cortical architecture is globally consistent across subjects of a given species, that is the same type of area and the same amount. However, the strong physiognomical variations of the cortex folds implies an important anatomical variability across individuals. Besides, studies of the cortical plasticity lead to the idea that the anatomy-function correspondence can vary across time for a given subject. Nonetheless, some fundamental retinotopic properties are stable: these are the fundations of the technique we present in this report.

First, let us define a central notion in any study of the visual system: the receptive field. Coarsely, it is "what a perceptual element sees", as a retinal ganglion cell or a cortical neuron. The (visual) receptive field of a cell generally corresponds to a small portion of surface in the fixation plane which, when a stimulation enters it, modifies the response of this cell. For example, in our experiment, this fixation plane is the screen the subjects look at (see figure 6).

Let us now state properties of the visual areas that define their retinotopic organization.

1) The neurons from different layers of a given cortical column share the same receptive field.

2) Two points close to each other in the visual field project closely on the retina. After various steps and following different paths (note that there is no consensus about these steps), these close retinal stimuli will be analyzed, inside a given area, in neighboring regions of the cortex (see the sketchy figure 3 and the more realistic figure 4 of the macaque monkey retinotopic map).
Thus, the primary visual cortex in humans (V1), anatomically in the occipital lobe around the calcarine sulcus, presents a retinotopic organization. The latter is approximately polar:
- when one moves along the cortical surface from a posterior to an anterior position in V1, the representation in the visual field moves smoothly from the center (fovea) to the surround. We say we vary the *eccentricity*.
- similarly, a displacement from the inferior limb of the calcarine to the superior limb results in the representation moving smoothly from the superior vertical meridian of the visual field to the inferior part of this vertical meridian. we say we vary the *polar angle*.
This type of representation can be found in various visual areas, as discussed later. This correspondance with polar coordinates allows us to define polar-coded stimuli (cf. paragraph 3.3.1).

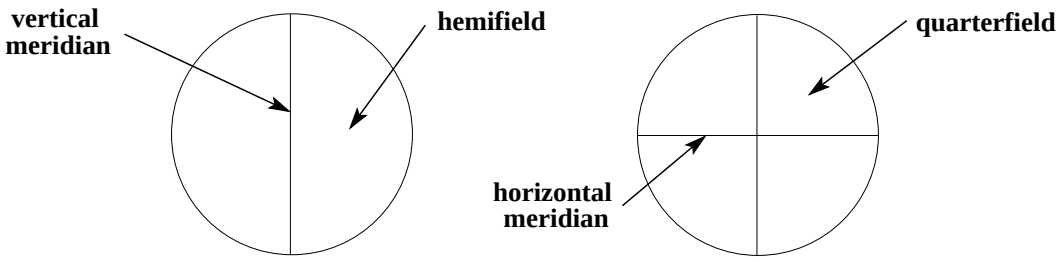

Figure 2: The visual field is split along the vertical meridian into two hemifields, each again split into two quarterfields along the horizontal meridian.

3) Two adjacent areas on the cortical surface (such as V1 and V2) differ with respect to their representation of the visual field. This is a crucial point for the differentiation of areas we are looking for. Indeed, some present a "reverse" or "mirror" representation, the visual field being projected on the cortical surface as if it was seen through a mirror, whereas others have a "normal" representation, consistent with the visual field spatial order. Thus the

representations change chirality[1] for two adjacent areas, a useful information we will take into account to detect the border between them.

These are the three fundamental retinotopic properties which allow us to differentiate and delineate the cortical areas of a given subject.

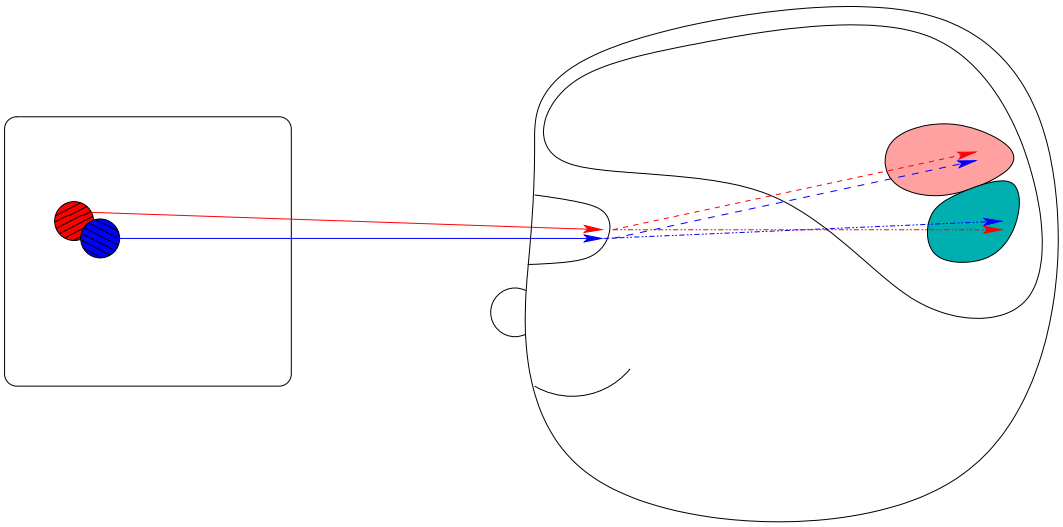

Figure 3: Schematic illustration of the retinotopic properties of the visual system in primates: continuity between the visual field and the cortical surface, inversion of the chirality between two adjacent areas.

2.2.1 Previous work

From previous studies of the cortical retinotopy in humans, in particular those of Engel et al. [7], Sereno et al. [17], Wandell [28], Warnking [29], we can infer the retinotopic structure classically found in the visual areas. First, as the two hemifields (the vertical separation of the visual field) split at the level of the optical chiasma, each hemisphere is only concerned with the visual information of its opposite hemifield. Second, as found in animals studies, some areas are split into to parts at the representation of the horizontal meridian. Hence the limits between adjacent areas correspond to horizontal or vertical meridians.

[1] In geometry, a figure is chiral (and said to have chirality) if it is not identical to its mirror image, or more particularly can't be mapped to its mirror images by rotations and translations alone, i.e. both figures are related like our left and right hands.

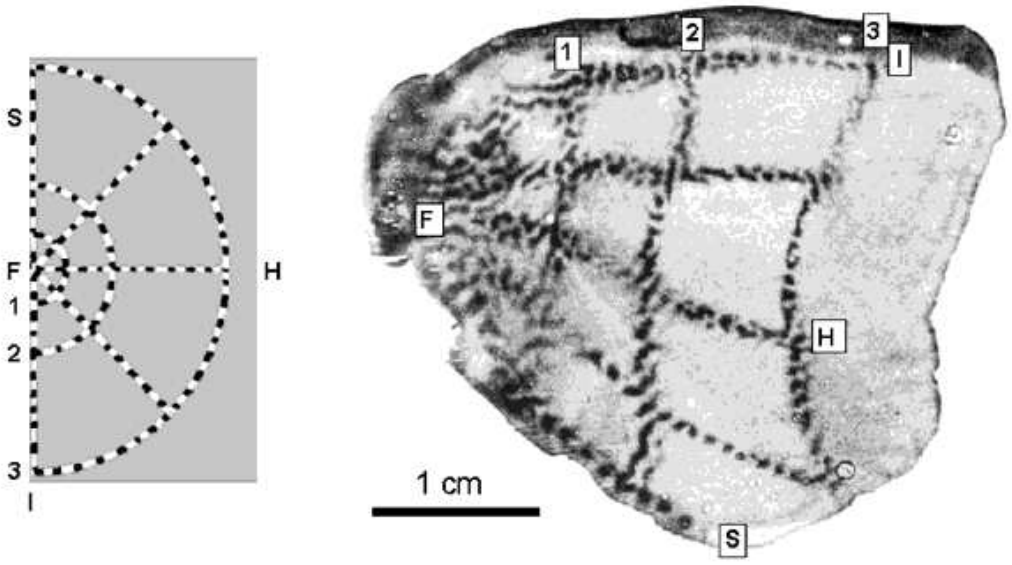

Figure 4: Global retinotopy in macaque visual cortex: a flickering stimulus (left) and its retinotopic representation in a flattened view of the layer 4C of V1 (right), revealed through CO staining. Reproduced from Tootell et al. [24]

V1 presents a retinotopy of the complete hemifield. The horizontal meridian projects to the fundus of the calcarine sulcus, the inferior quarterfield on the upper part of the calcarine and the superior quarterfield on its lower part. The vertical meridians delimit each side of V1 with V2v and V2d, the two fragments of area V2. The latter represent the upper and lower quarterfields respectively. In V2, the representation is reversed with respect to V1 (which is "mirror"), so that the border of them respectively with the so-called area VP and V3 coincide with the horizontal meridian. Once again, the representation reverses for V3 and VP, until the vertical meridian, after which an other inversion takes places for V3A dorsally and V4 ventrally. Figure 5 illustrates this description, which we discuss in section 6.1.2.

We therefore see how the knowledge about the retinotopy on the cortical surface can be sufficient to delineate the visual areas. In the next section, we describe the experimental protocole that we have developed in order to build the retinotopic maps of a human subject using fMRI.

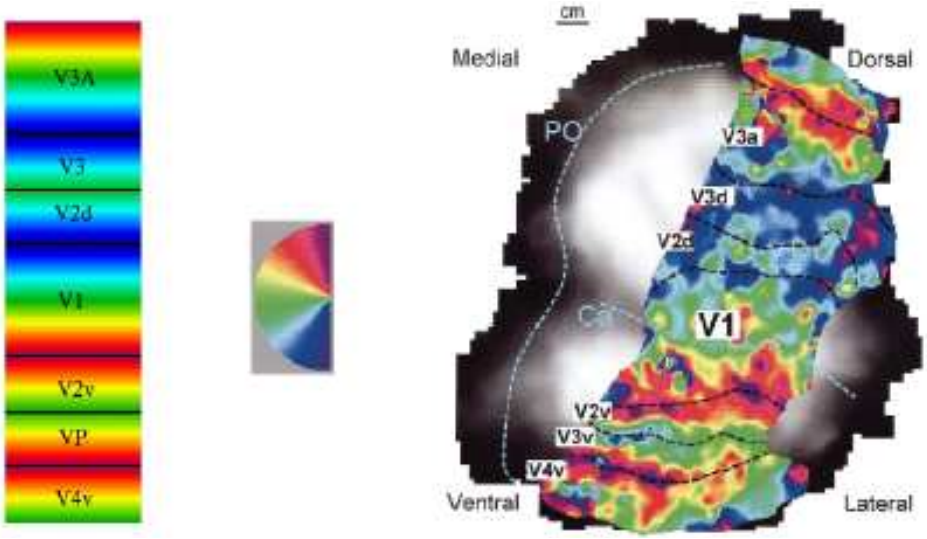

Figure 5: Polar angle retinotopy of the right hemisphere, i.e. the left visual hemifield. The left-hand side of the figure illustrates the spatial arrangement of differents areas and their retinotopy, the hemi-circle at the center corresponding to the color code employed for each angle of the visual field (from Warnking [29]). The right-hand side of the figure shows results obtained from human fMRI on an unfolded cortical surface by Pr.Wandell's team, V3v and V3d corresponding to V3 et VP in the text and on the left-hand side of the figure respectively.

3 Experimental protocol

Taking into account the retinotopic properties of the visual cortex we just briefly described and building on previously published work on the subject, we now define our experimental paradigm and our stimuli.

3.1 The subject

No constrains are applied to the subject, except those induced by the MR scanner: a complete absence of metal parts in the body, including vascular clips, neuronal implants, pacemakers, etc...This also excludes glasses, but lenses could replace them if any correction is needed.
As a rule of thumb, the idea for any global non-pathologic study is to use healthy right and left-handed men and women. This is the guideline we followed in order to obtain the results we present in this report.

3.2 The scanner and the presentation device

The MRI scanner we used is located at la Timone fMRI center[2] in Marseille, France. It is a BRUCKER MEDSPEC 30/80 AVANCE, with a 3T magnet and a body coil.
The subject lies inside the coil, with an antenna around his head. The visual stimuli are projected from a video-projector inside the magnet room, protected from the magnetic field in a Faraday cage. A mirror allows to project the image on a screen inside the coil. The subject sees this screen by means of mirror placed above his/her eyes (see figure 6).
The stimuli are sent to the video-projector from a PC at a frequency of 72Hz. The video starts synchronously with the scanner, triggered by the first functional volume acquired. Actually, the first volumes are classically discarded from the analysis (typically corresponding to 10 seconds) to allow the magnetization to stabilize to a steady state, the stimulation of interest therefore starts after a few volumes have been acquired.

3.3 Paradigm

Classically, the paradigm in fMRI consists in a series of temporal stimuli the subject watches and the tasks he performs.

[2] http://irmfmrs.free.fr

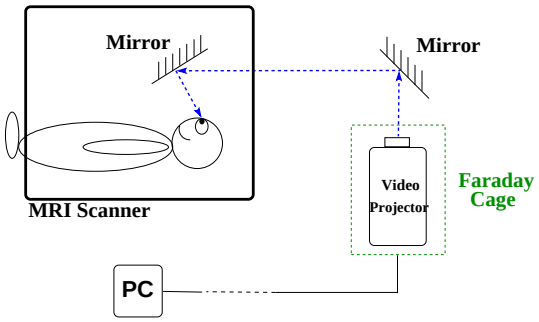

Figure 6: The projection system of our experimental setup

3.3.1 The stimuli

The stimuli we used were programmed in Matlab to generate a video sequence in avi format. A number of parameters were adjustable.
The aim is to stimulate locally and periodically the visual field of the subject whose gaze stays fixated at the central point. The basic pattern of our stimuli is a radial checkerboard similar to those described in the litterature (e.g. [29], [17]). The pattern we used consists in squares distributed in the radial and the polar dimensions. It takes into account the cortical magnification, the squares's size is thus increasing with the eccentricity.
We finally require two families of stimulus:
- The *wedge* is a conical sector of 80 degrees rotating around the central fixation point. This stimulus moves in discrete 20 degrees steps in the visual field in a circular clockwise or anti-clockwise fashion, thus leading to 18 different positions for a complete 360 degrees rotation (see figure 7).
- The *ring* is an annulus centered at the fixation point, its size varying with respect to the

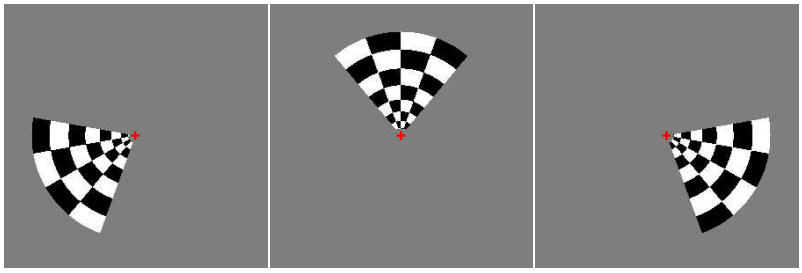

Figure 7: The "wedge" stimulus seen in different positions. It encodes the polar angle coordinate θ in the visual field.

eccentricity. Like the wedge it also has two directions of rotation, contraction and expansion;

a complete rotation is achieved in 18 distinct steps. When the annulus reaches its maximal eccentricity (respectively minimal), it is replaced by an annulus at minimal (resp. maximal) eccentricity, with an intermediate position of coexistence (cf. the right image of figure 8). This wrapping around allows to have a close to continuous motion of the stimulus.

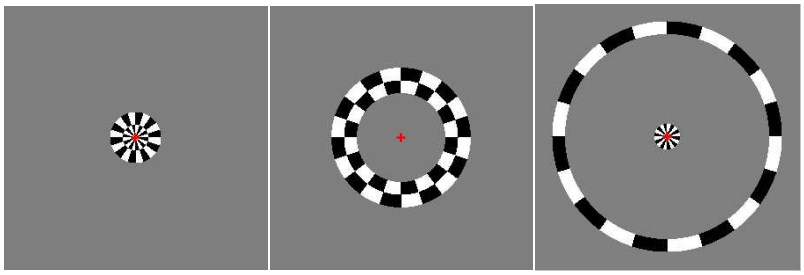

Figure 8: The "ring" stimulus seen in differents positions. It encodes the eccentriciy coordinate ρ in the visual field.

The checkerboard pattern of these stimuli flickers (at 18Hz in our setup) in order to insure a good neuronal response. Indeed, most of the receptive fields cells in the retina and the Lateral Geniculate Nucleus -the main inputs for the first visual cortical areas- consist of two antagonistic regions, the best response of the cells being obtained with a luminance local contrast between their center and surround. This checkerboard pattern is superimposed on a mid grey-level equiluminant background to let the cells whose receptive fields do not fall on the checkerboard at rest.
The size of our videos is 300x300 pixels, leading to a 20.9x20.9 degrees display. This size is for the moment limited by the size of the coil and the visual stimulation setup. The extent of the radial maximum reached by our stimuli is 280x280 pixels, giving a maximum radial opening in the visual field of 19.5 degrees.
Thus, in terms of polar coordinates, the *wedge* stimulus encodes the polar angle component whereas the *ring* encodes the radial component. The complete visual field is then completely covered, and these two families of stimuli carry complementary information with respect to the simulation of the visual field.
For each position of the stimulus, we scan a functional volume, yielding at the end of each stimulation a temporal series S_n of images.

3.3.2 Stimulus optimization

Our aim is to design an experimental setup allowing a quick and reliable retinotopic mapping to accurately delineate the visual areas to be used in further fMRI experiments. We thus varied two different parameters of our stimulus: the number of sectors in the wedge and the number of complete rotations (or cycles). The results were presented in [33] and are described below.

Unifield VS bifield wedge We also used a bifield wedge for two reasons:
- The experiment duration could be divided by two, as we stimulate two distinct portions of the visual field, thus different cortical locations
- the fixation of the center of the visual field is easier with a symetrical stimulus.

The results are shown and discussed in the results section, paragraph 6.1.2.

3.4 Data acquisition

Two types of data are needed to build retinotopic maps: an anatomical image and the functional volumes.

3.4.1 Anatomical data

The acquisition of the cerebral anatomy of a given subject was done through a 3D-gradient echo sequence with inversion-recovery. The technical caracteristics of the latter are the following:
- Echo-Time (TE): 5ms
- Repetition-Time (RT): 25msec
- Inversion-Time (IT): 800ms
- Field of view: 256x192x192 mm^3
- Acquisition matrix: 256x192x104 (for a resolution of 1x1x1.5 mm^3)
- Reconstruction matrix: 256x256x128 (for a resolution of 1x0.75x1.22 mm^3)

This leads to a 15 minutes sequence to get a high resolution anatomical image.

3.4.2 Functional data

The functional images were acquired with an Echo-Planar sequence. In order to reduce the repetition time (RT) and thus the time needed to acquire a functional image, we have restricted our functional scans to the occipital region of the brain, rather than the complete head. We first started with 18 3mm thick slices with an inplane resolution of 3mmx3mm, oriented approximately perpendicular to the calcarine sulcus. The corresponding TR was 1.5s ($18 \times 83.33ms$). We then used a 2x2x2mm^3 resolution, using 20 slices to cover a sufficient portion of the brain. This last sequence requires 103ms to acquire a slice, leading to a RT of 2060ms. This RT was slightly increased (to 2111ms) for each image in order to get a good synchronization between the presentation device (refreshing at 72Hz and showing 18 different images per second) and the volumes acquisition. Indeed, within a TR of 2111ms, we can present $18 \times 2.111 \approx 38$ different images (whereas 18*2.060 does not lead to an integer number of images). Thus, for 4 complete rotations of the stimulus, the duration is 152 seconds, 2mn32s (the ring in one direction), and 5mn04s for 8 complete rotations (the wedge in one direction).

Globally, we are then able to acquire all the functional volumes needed for our retinotopic mapping in 20 minutes including the scans acquired without any stimulation (signal stabilization) and the time for the subject to rest between two stimuli.

4 Functional data analysis

A functional MRI data analysis typically comprises the following steps:
1) The pre-processings for correcting possible defects in the acquisition (head motion, acquisitions gaps between slices,...) and performing some spatial and temporal smoothing of the data.
2) The statistical analysis: it allows to assess the volume's elements whose activity is correlated with the experimental paradigm.
3) The study of the results: for confronting quantitative statistical results to qualitative criteria for example.

In the following, the functional series will be viewed as 4D data (3 spatial dimensions + time). Each volume acquired within a given RT is seen as an image, and a set of volumes acquired in a row is called a run or a session.

4.1 Preprocessing

To begin the functional data analysis, we apply different preprocessing steps; indeed, only the BOLD signal is of interest for activation detection, any other signal is then considered as noise and should, as far as possible, be removed.

It is necessary to remove the first images from the temporal series. We indeed always take a few images (typically 5 RT in our case, about 10 seconds) during the MR signal stabilization phase; the latter, depending on the scanner and the sequence used, is known to give rise to many artefacts in the images (mainly abnormal high level values in the signal). There is of course no visual stimulation of interest during these few scans. We then apply our preprocessing to the remaining images.

4.1.1 Motion correction

The subject's head motion during a scanning session is unavoidable and may induce artefacts, leading to a loss of activations or, worst, to false positives, that is to voxels considered as activated whereas they are actually not. All subsequent analysis or processing on series comprising motion could be invalid as we cannot identify properly the signal and the voxels. We proceed in two steps: first we estimate the motion, second we decide to correct for it or not.
The coregistration, allowing an estimation of the motion, was at first done using the standard SPM *realign* function. A reference image I_R is designated by the user and the other images are registered with it using a rigid transformation T. A rigid displacement is composed of a translation and a rotation, thus 6 parameters for a 3D image. The error E between the reference image I_R and the image I_i to realign is the sum of the squares of the intensity

differences of each voxel x:

$$E^2 = \sum_x (I_R(x) - I_i(T(x)))^2$$

E is minimized with respect to T using a least squares technique. At the end of this step, we can visualize the corrections attached to each 3D image, and thus have an estimation of the subject's motion (cf. figure 9).

The estimated motion was in general very small, which raised the question of the need for such a correction. Following Freire et al. [8], we considered that motion was negligible when the estimated motion was less than the voxel size. We furthermore used a different algorithm than the standard from SPM, based on a slightly different similarity measure[3], to estimate the motion. This algorithm leads to a more robust coregistration of the functional volumes.

4.1.2 Anatomical/Functional images alignement

As we finally display the results of the functional images analysis on a model of the cortex derived from the anatomical image, the alignment between functional and anatomical scans is important. There are two main sources for disalignement:
- the subject moved the head between the anatomical and the functional scans. This should be well corrected by a rigid deformation (rotation and translation).
- as it is often reported in high field Echo Planar Images (EPIs), there could be distorsions in the functional images that might not be well corrected for by a rigid deformation.
We adressed this question using a non-rigid deformation algorithm, estimating a dense deformation field to be applied to the functional images. We used an algorithm developed in the laboratory [2]. Globally, the estimated deformation field was negligible with respect to voxels size, and we decided not to apply the correction. The realignement was nonetheless assessed visually using SPM's chek_reg function.

4.1.3 Correction of the inter-slice gap or *slice-timing*

A volume is made of different slices that are not acquired at the same time during the scanning process. Thus, in the case of the interlaced sequences that as we use in our experiments, a time discrepancy of the magnitude of half the RT can be present between two spatially adjacent slices of the same volume. A temporal analysis of the raw images should take into account these differences. A simple solution is to correct for this discrepancy to be able to apply the same statistical analysis to each slice, then considered as acquired at the same point in time.
This pre-processing is done by the *Slice-Timing* method of the SPM software, which moves some slices in time to get a volume considered to be acquired at the same time point. This correction works with a temporal interpolation of the time series at each slice using an

[3]The program we used can be found at http://www-sop.inria.fr/epidaure/software/INRIAlign/

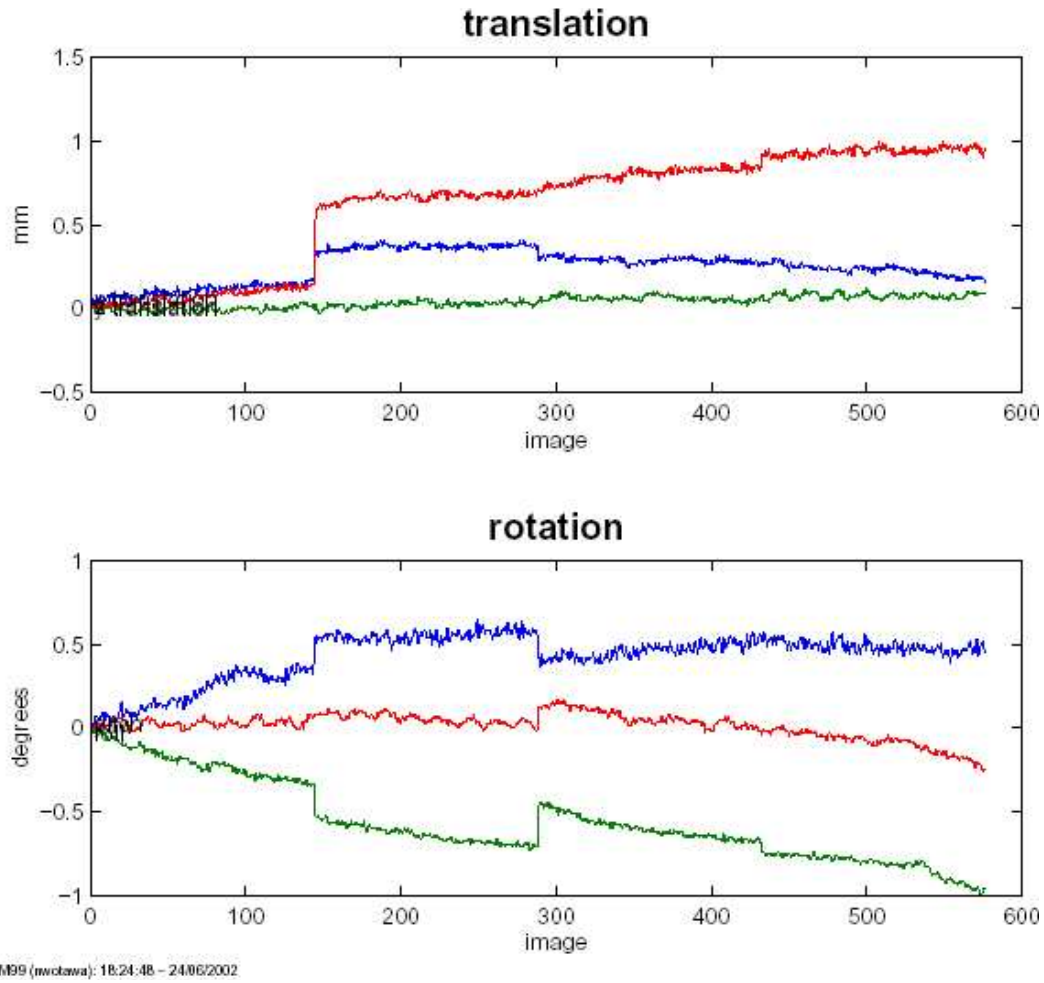

Figure 9: An example of file produced by SPM during a motion correction of the functional images. The upper graph shows the estimated values of the 3 coordinates of translation directions for each image, the lower one shows the 3 estimated coordinates values of the rotation motion computed. We notice that the motion is larger between each session of 162 images, corresponding to a certain kind of stimulus (for example : ring expanding for the 162 first scans, then contracting for the next 162,...), which seems consistent with motion of the subject waiting between two sessions. Note that this was not specified to the algorithm during the motion correction: the estimation seems credible.

interpolation with a sinc function. The algorithm then realigns each slice by changing the

phase of the signal taken in the Fourier space. This method assumes there is no information of interest beyond the Nyquist frequency, i.e. the sampling frequency divided by two. The output of the algorithm is a temporal series of images where each slice would have been acquired at the beginning of the RT.
In the retinotopic mapping experiment, we can avoid this preprocessing which has no effect on the phase estimation procedure presented below (cf. paragraph 4.5).

4.1.4 Spatial smoothing

Although surprising at first, a spatial smoothing is commonly applied to fMRI images [9]. The main reason is to increase the signal to noise ratio (SNR), by reducing the effect of spatially uncorrelated noise. This smoothing also increases the validity of the assumptions used during the statistical analysis done by SPM, i.e. the residuals of the regression model can be treated as a Gaussian random field. Lastly, this also helps insuring a better spatial overlap between activations across differents subjects in multi-subjects analysis.
The Gaussian kernel we typically use has a Full Width at Half Maximum (FWHM[4]) equal to 1.5 times the voxel size. In our experiments, this step highly increases the quality of the resulting retinotopic maps.
However, this smoothing is not optimal as it does not take into account the geometry of the cortical surface, thus mixing voxels from different tissues. We have implemented another approach enabling a smoothing along the cortical surface. This method and the results are presented elsewhere in [32].

4.1.5 Temporal filtering

Correction of the scanner trend Instabilities of some scanner equipments give rise to a trend in the signal baseline. Furthermore, aliased physiologically induced effects (cardiac, breathing,...) also introduce low frequency components in the signal. These confounds can easily be removed applying a high-pass filter during the statistical analysis of the voxels time series. The cutting period (the inverse of the cutting frequency) was chosen to depend on the interval of time separating two equivalent stimulations in a given session (the stimulus period in our experiments). This interval is classically called the Stimulus Onset Asynchrony (SOA). We typically used 2.5 times this value (expressed in seconds) to remove every frequencies lower than $\frac{1}{2.5SOA}$.

Low pass filtering To insure better estimates of the statistical model parameters used in the analysis done at the next step (see part 4.2), a temporal smoothing is performed on the data to consider as known the residual time series autocorrelations. We use a simple Gaussian temporal filtering on the data that will be taken into account in the statistical

[4]The FWHM is linked to the standard deviation σ of the gaussian kernel by the formula:

$$FWHM = \sigma\sqrt{8ln(2)}$$

analysis.

We have presented here the different steps of preprocessing we have considered for our functional images analysis. The problem of choosing which one to use was adressed by the following algorithm:
1. Run the motion correction algorithm

   If the global motion is over the voxel size, apply the coregistration

   Else, ignore the coregistration (keep the original data)

2. Spatially smooth the data with a FWHM equals to 1.5 times the voxel size

3. High-pass filter the resulting time series to correct the scanner trend. The cutting period is proportional to the Stimulus Onset Asynchrony.

4. Temporal low pass filter to remove high frequencies noise. Actually, those steps 3 and 4 are performed within SPM, through the batches described later (see Appendix A).

After this preprocessing, we can go to the voxels analysis using a model linked to our paradigm. We describe this analysis in the next section.

4.2 Statistical analysis

This stage aims at establishing which functional voxels are correlated to our stimulation. The method we use can be qualified as:
- univariate: the analysis is performed independently for each voxel (as opposed to multivariate analysis which considers all voxels simultaneously)
- differential: answers to a binary question (activated/not activated)
- parametric: some assumptions are made about the linearity of the response with regard to the stimulation and about the structure of image noise.

As customary in SPM analyses, we describe in this section the three main steps in the statistical analysis: the model specification, the model parameters estimation and the definition and estimation of statistical tests to reveal the activated zones.

4.2.1 Specification of a linear statistical model

A classical method, implemented in SPM99, to analyze MR functional images is to use a linear model, applied at each voxel to measure the hemodynamic response ([9]). In this experiment, we use a periodic paradigm which we obviously take into account in our model definition.

In the following description, we consider a given voxel v and a given session (e.g. *clockwise wedge*) of length T. The time series of v is noted $\{S_v(i)\}_{i=0\dots T-1}$.
Based on our stimulus paradigm (paragraph 3.3.1) and the retinotopic properties (paragraph 2.2), the voxel should only show an activity signal when the stimulus position overlaps the receptive fields of the neurons in this voxel. As our stimuli are moving periodically and as far as the response is linear (which is reasonable if two consecutive stimulations are sufficiently separated in time), the observed signal should also be periodic, with a frequency equal to the stimulation frequency, noted k_0. It is therefore natural to study the discrete Fourier transform of our time series:

$$S_v(t) = \sum_{k=0}^{T-1} c_v(k) e^{\frac{2i\pi kt}{T}} \qquad \forall t \in \{0, \cdots, T-1\} \tag{1}$$

where $c_v(k) = \frac{1}{T} \sum_{t=0}^{T-1} S_v(t) e^{-\frac{2i\pi kt}{T}} \qquad \forall\, k \in \{0, \cdots, T-1\}$

A simple relation links the stimulus frequency k_0 to ω_0, the stimulus pulsation[5]:

$$\omega_0 = \frac{2k_0\pi}{T}$$

We are interested in the part of the signal at the frequency k_0. The equation (1) could be written:

$$\begin{array}{lll} \forall t \in \{0, \cdots, T-1\}, & S_v(t) & = \beta_{v,0} + c_v(k_0) e^{\frac{2i\pi k_0 t}{T}} + \epsilon_v(t) \\ & & = \beta_{v,0} + \beta_{v,1}\cos(\omega_0 t) + \beta_{v,2}\sin(\omega_0 t)] + \epsilon_v(t) \end{array} \tag{2}$$

$\beta_{v,0}$ is the mean of the temporal signal. Detailing the formulas, it yealds:

$$\left\{ \begin{array}{lcccccccc} S_v(0) & = & \beta_{v,0} & + & \beta_{v,1} cos(\omega_0 \times 0) & + & \beta_{v,2} sin(\omega_0 \times 0) & + & \epsilon_v(0) \\ & \vdots & & & & & & & \\ S_v(T-1) & = & \beta_{v,0} & + & \beta_{v,1} cos(\omega_0 \times (T-1)) & + & \beta_{v,2} sin(\omega_0 \times (T-1)) & + & \epsilon_v(T-1) \end{array} \right.$$

We therefore define two temporal regressors:

$$X_1 = \begin{pmatrix} \cos(\omega_0 \times 0) \\ \cos(\omega_0 \times 1) \\ \vdots \\ \cos(\omega_0 \times (T-1)) \end{pmatrix} \qquad and \qquad X_2 = \begin{pmatrix} \sin(\omega_0 \times 0) \\ \sin(\omega_0 \times 1) \\ \vdots \\ \sin(\omega_0 \times (T-1)) \end{pmatrix} \tag{3}$$

[5] The pulsation ω_0, expressed in radian per second, is linked to the stimulation period T_0, expressed in seconds, by the simple relation: $\omega_0 = \frac{2\pi}{T_0}$

so that:

$$S_v = \beta_{v,0} X_0 + \beta_{v,1} X_1 + \beta_{v,2} X_2 + \mathcal{E}_v \tag{4}$$

where :
- X_0 is the temporally constant regressor, i.e. a unity vector of dimension T (all coordinates equal to 1)
- $\mathcal{E}_v \in \mathbb{R}^T$ is the residual error, i.e the part of the signal not explained by our model, corresponding to all frequencies different from k_0.

Equation (4) can be written in matrix form:

$$S_v = X B_v + \mathcal{E}_v \tag{5}$$

The $\epsilon_v(i)$ are supposed to be independently and identically distributed (*iid*), following a $\mathcal{N}(0, \sigma^2)$ law. This assumption is justified thanks to the high-pass temporal filter applied during the preprocessing (see paragraph 4.1.5), which removes temporal autocorrelations. The constant regressor does not play any special role in the remainder. The vectors X_1 and X_2 are decorrelated, as $Cov(X_1, X_2) = 0$. Furthermore, the regressors are decorrelated from one session to the other as they are not applied to the same data.
We can get a graphical description of our model via SPM, as shown in figure 10, in particular with the correlations between the different model regressors X_i.

Lastly, within this model we will look closely at two parameters:
- $\|c_v(k_0)\|^2 = \beta_{v,1}^2 + \beta_{v,2}^2$ coding the strength of the frequency k_0 in the voxel time course,
- $\phi = \arctan\left(\frac{\beta_{v,2}}{\beta_{v,1}}\right)$ which is an estimator of the fMRI signal phase.

The model is applied to each stimulus, so that for each subject we define 4 models (formally identical) with 2 regressors each (ignoring the constant regressor).

4.3 Model parameters estimation

We are now faced with a classical problem of estimating our regressors coefficients from a functional data temporal series. This boils down to finding the values of the $\beta_{v,i}$ minimizing the residual error E_v. The **ordinary least square method** is applied. We therefore have to solve the following problem (cf. equation (5)):

$$\underset{B_v}{Min}\, \mathcal{E} = \| E_v \|^2 = \| S_v - X B_v \|^2 \tag{6}$$

Depending upon the model, the computed values can be unique or not. As our matrix X is full rank, meaning that no regressor is a linear combination of the others, the estimations are unique and the results are thus reliable. The calculation to be done is the following (the

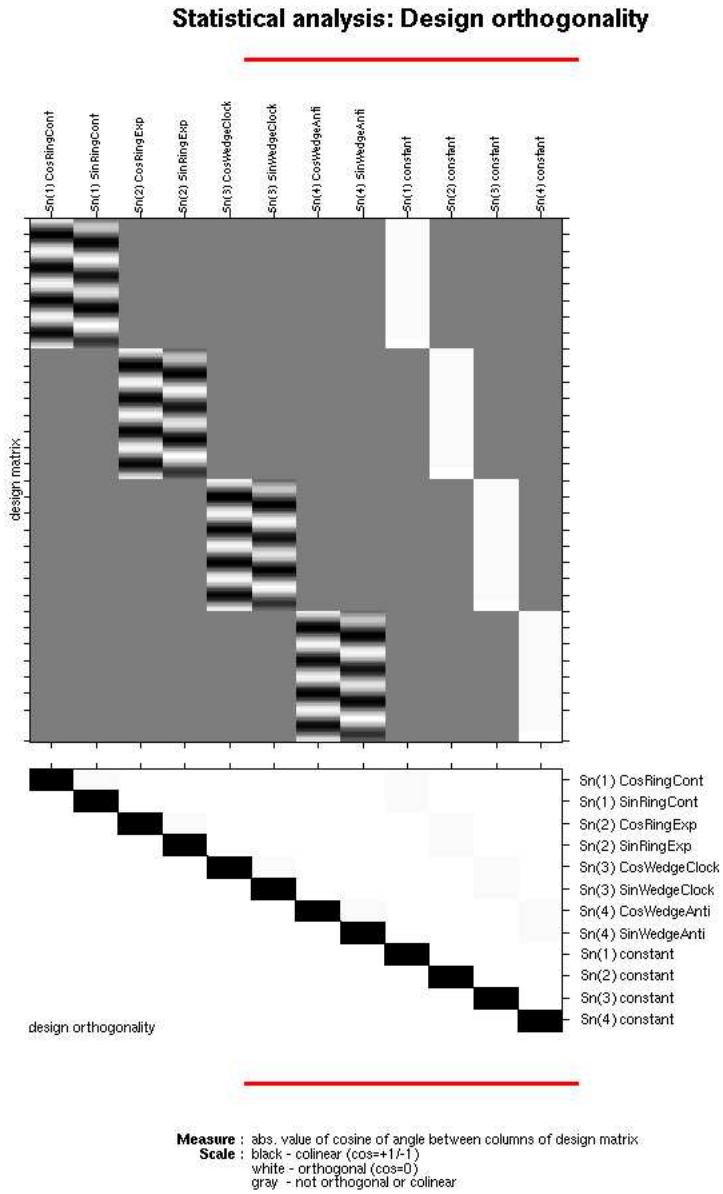

Figure 10: Graphical description of the statistical model. The upper graph represents the SPM design matrix, in which each column corresponds to the values of a given regressor across scans. The 4 right columns are the constant regressors. The lower graphic shows the orthogonality of the design matrix, i.e. the correlation between the regressors of our model. They all appear to be independant as expected (white color).

v index is dropped to simplify notations, but this is done for each voxel):

$$\begin{aligned}\mathcal{E} &= \sum_{t=0}^{T-1} \epsilon(t)^2 \\ &= \sum_{t=0}^{T-1} (S(t) - \beta_0 - \beta_1 x_1(t) - \beta_2 x_2(t))^2\end{aligned}$$

A necessary condition (and also sufficient as we are considering a quadratic positive definite form) for minimizing equation (6) is :

$$\frac{\partial \mathcal{E}}{\partial \beta j} = 2 \sum_{t=0}^{T-1} (-x_{ij})(Y_i - \beta_0 - \beta_1 x_1 - \beta_2 x_2) = 0 \qquad \forall j \in \{0, 1, 2\}$$

This corresponds, up to a scale factor of 2, to the j-th row of the equation $X^\top Y = (X^\top X)B$, called the normal equation.
Thus, $(X^\top X)$ being invertible (as the matrix X is of full rank), the least square estimation of B is:

$$\hat{B} = (X^\top X)^{-1} X^\top Y$$

Under the asssumption of Gaussianity for the residuals and assuming besides their independence, this estimation is the one of maximum likelihood and also the best linear un-biased estimation of B. In other words, this means that among all estimators that are linear combinations of the data with a mean equal to the true value of the parameters ($\mathbb{E}(\hat{B}) = B$), its variance is minimum.

4.4 Statistical tests

This step consists in producing statistical tests on the parameters β estimated in the previous paragraph in order to compare the relative contributions of each regressor and to decide whether a given voxel activity is explained or not by our model. In our case, we are led to perform an F-test on the β coefficients. We will deduce from this test a mask of the voxels to keep in the last step.
In our study, we defined three slightly different tests that can be applied to every voxel.

Global test
The first test, quite classical, allows to answer the question: "is our global model of regressors accounting well for the signal variations at the voxel considered?". It is called "effect of interest" in the SPM language. The constant regressors beeing excluded, we test for the null hypothesis:

$$(H_0) : \beta_1 = 0 \text{ and } \beta_2 = 0 \text{ and } ... \text{ and } \beta_8 = 0$$

H_0 is equivalent to the nullity of the norm of the coefficients $c_v(k_0)$, implying that no signal contains any significant energy at the fundamental frequency of the stimulus.

The alternative hypothesis is:

$$(\overline{H_0}) : \exists\, i \in \{1, ..., 8\} \quad / \quad \beta_i \neq 0$$

meaning that our model "explains" at least a significant part of the signal, or in frequency terms that a significant part of the signal contains energy at the fundamental frequency of stimulation.

To be able to do a statistical test, we need an additional assumption on the β_i: they are supposed to follow a Gaussian law $\mathcal{N}(0, \sigma^{'})$. They are therefore all independent (as they come from Fourier decompositions) and Gaussian. Then: $\sum_{i=1}^{8} \beta_i^2 \rightsquigarrow \sigma^{'2}\chi^2(8)$.
The global model residuals variance is estimated with the sum of the residuals divided by their degrees of freedom. By assumption, $\epsilon_i \rightsquigarrow \mathcal{N}(0, \sigma)$, we then have:

$$\frac{1}{T-q}\sum_{t=0}^{T-1} \epsilon_t^2 = \frac{\mathcal{E}^\top \mathcal{E}}{T-q} \rightsquigarrow \sigma^2 \frac{\chi^2_{T-q}}{T-q}$$

where $T - q$ is the number of degrees of freedom remaining in ϵ. Here, q=12 (the 8 β_i plus the 4 constant regressors).
The respective variances of the residuals and the β_i are identical ($\sigma = \sigma^{'}$), as they correspond to the global variance of the signal S_v. Besides, the residuals and the β are independant thanks to the Fourier decomposition of the signal (equation 1), the Fourier coefficients being independent.

The statistical test thus relies on:

$$\hat{F} = \frac{\frac{\sum_{i=1}^{8} \beta_i^2}{8}}{\frac{\mathcal{E}^T\mathcal{E}}{T-12}}$$

This ratio is estimated then compared to the p-value f of the corresponding Fisher law $\mathcal{F}(8, T-12)$[6]. Any voxel verifying $\hat{F} > f$ (unilateral right test) does not follow H_0, so its signal is partly explained by our model. Such a voxel will be part of the "effect of interest" mask. Figure 11 presents typical $\hat{F}$ values for the *wedge* stimulus.

Specific tests
The other two contrasts we defined are more "local" contrasts in the sense that they are linked

[6]It shall be noted that the way SPM computes the degrees of freedom is slightly more complicated because it takes into account the high-pass and low pass filtering applied by SPM; this leads to non integer values for these degrees of freedom, but the approximation used here is sufficient, the threshold values computed being very close to the theoretical values.

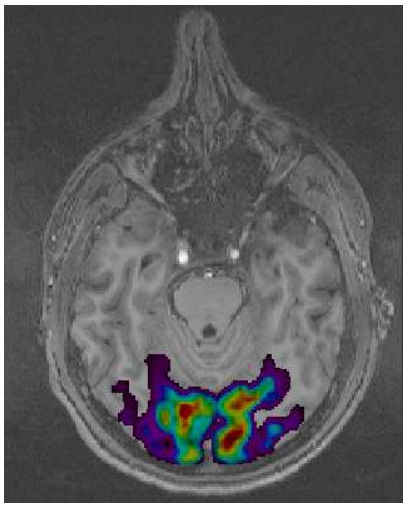

Figure 11: An axial slice of the values of the statistics $\hat{F}$ for the *wedge* stimulus, in a global test. The values under the theoretical p-value computed for $p = 0.01$ are discarded. The colored voxels are those forming the analysis mask.

to only one familly of stimulus (*wedge* or *ring*). They respectively test the assumptions[7]

$$(H_1^w) : \beta_1^{wd} = 0 \text{ and } \beta_2^{wd} = 0 \text{ and } \beta_1^{wi} = 0 \text{ and } \beta_2^{wi} = 0$$

and

$$(H_1^r) : \beta_1^{rd} = 0 \text{ and } \beta_2^{rd} = 0 \text{ and } \beta_2^{ri} = 0 \text{ and } \beta_2^{ri} = 0$$

They allow to check if the respective model of each type of stimulus explains well the observed signal. The corresponding statistical tests are, as previously, F statistics, this time of law $\mathcal{F}(4, T-6)$. Specific "wedge" and "ring" masks can then be derived.

Globally, we prefer to check our results with each specific mask separately, as the two families of stimuli can be viewed as independent. We however considered the global mask as neurons activated by one familly of stimulus (e.g. the "wedge") should also be activated by the other (e.g. the "ring"), the portion of the visual field globally covered by both stimuli beeing strictly identical.

We wrote a serie of scripts to automate this computing steps using SPM99 (defining the model by hand is time consuming and repetitive if you scan many subjects). Those scripts define the model, the contrasts and statistics in the SPM99 syntax, call the SPM99 function

[7] wd, wi and rd, ri are respectively notations for *wedge direct* or *indirect* and *ring direct* or *indirect*.

used for the regression step and the statistics to estimate. An example of those files and an explanation of the parameters to tune for their usage is given in Appendix A.

Interpolation in the anatomical referential
At this stage, we apply an interpolation of the resulting β and mask images in the referential and format of the anatomical image (see section 5). This is useful to display easely the following results on the meshes resulting from the anatomical segmentation.

4.5 Angular values computation

The last step in the functional data analysis consists in recovering, for each voxel included in the statistical mask computed previously, the phase of the signal, which is linked to the stimulus position that induced the voxel's response.
According to our paradigm and the construction of our model, this would be relatively straightforward without the hemodynamic filtering. Indeed, as seen previously, $\phi = arctan(\frac{\beta_2}{\beta_1})$ is an estimator of the signal phase, corresponding to a unique stimulus position in the visual field. But the response we are faced with is filtered and delayed by the hemodynamic response, making the underlying position estimation more difficult. However, taking advantage of the two directions of rotation for each familly of stimulus allows to estimate, *for each voxel*, this hemodynamic delay.

Let us consider a given supra-threshold voxel v, and define the following notations:
- θ^+ (respectively θ^-) is the *angle* coding for the position of the stimulus rotating positively (resp. negatively) in the visual field.
- ϕ^+ (resp. ϕ^-) is the periodic signal estimated *phase* for the stimulus in positive (resp. negative) rotation.
- τ^+ (resp. τ^-) is the "expected" signal phase, i.e. the delay of the neuronal response (close to zero at our temporal scale), linked with the position θ^+ (resp. θ^-) of the stimulus by the relation $\theta^+ = \tau^+\omega_0$ (resp. $\theta^- = \tau^-\omega_0$) where ω_0 is the stimulus pulsation. We have the relation $\tau^+ = 2\pi - \tau^-$.
- t_h is a delay in the recorded BOLD response, that is the hemodynamic delay at the voxel v plus the acquisition delay linked to the corresponding slice in the volume. We assume that this delay is identical for the two directions of rotations of the same stimulus, which appears to be reasonable[8]. By the way, this delay could also comprise some physiological aspects as lateral propagation effects that could reasonably be assumed to be identical in both directions of rotation.

[8]Notice that this assumption is valid concerning the slice acquisition delay because our stimulus time course is precisely synchronized with the volumes acquisition, making each slice acquired with the same delay with respect to the stimulus change of position in both directions of rotation.

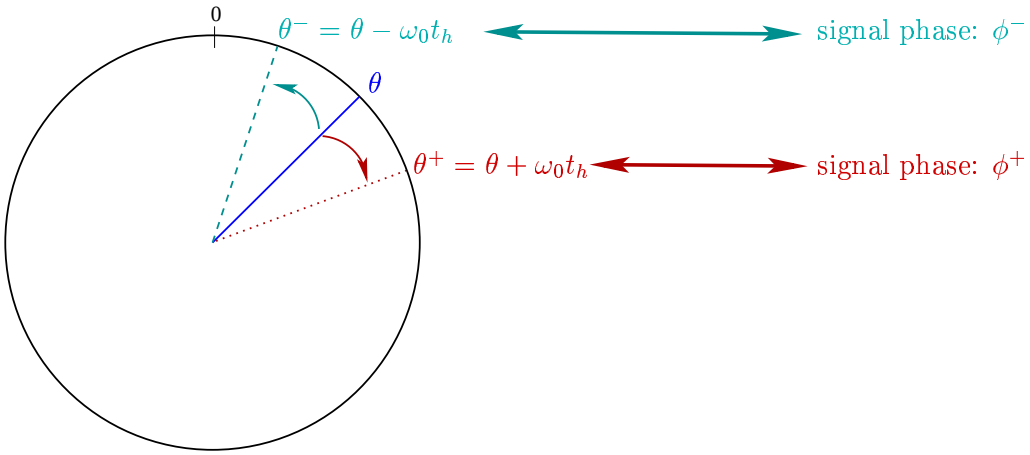

Figure 12: Description of the stimulus positions in the visual field linked to the periodic signal measured phases. This sketch refers to the *wedge* stimulus. The red (respectively green) color corresponds to a positive (resp. negative) rotation. θ is the *angle* corresponding to the stimulus position in the visual field inducing a simulation of the neurones included in the voxel considered, t_h is mainly due to the hemodynamic delay of this voxel, ω_0 the stimulus pulsation. The conjunction of the estimated *phases* in the periodical signals, ϕ^+ and ϕ^-, allows to evaluate the values of θ and t_h.

We thus have :

$$\begin{aligned}\phi^+ &= \tau^+ + t_h \\ &= \frac{\theta^+}{\omega_0} + t_h\end{aligned}$$

$$\begin{aligned}\phi^- &= \tau^- + t_h \\ &= 2\pi - \tau^+ + t_h \\ &= 2\pi - \frac{\theta+}{\omega_0} + t_h\end{aligned}$$

We can remove the term 2π, useless here as our results will in fine be defined modulo 2π. So:

$$t_h = \frac{\phi^+ + \phi^-}{2} \tag{7}$$

$$\theta^+ = \frac{\omega_0(\tau^+ - \tau^-)}{2} \tag{8}$$

The hemodynamic delay is defined modulo π by equation (7), but the ambiguity is removed by the fact that the stimulus frequency is low enough to allow the hemodynamic delay value to be, expressed in terms of stimulus position angle, between 0 and π (modulo 2π).
At the end of this step, we are thus able to evaluate at each voxel concerned by our stimulus the value of the angle (thus the underlying position) of the stimulus giving rise to its activity.

As for the "statistical model" part, this phase estimation step was automated using a Matlab code. It leans on the SPM99 interface to select the images (that is the β images, the F-values image and the SPM mask). This script furthermore avoids some problems we were faced with using the "imcalc" function implemented in SPM which allows to apply any mathematical formula to an image. Indeed, this SPM99 code restricts the resulting image to be of integer values, sometimes leading to numerical problems and loss of information despite of a trick called the scalefactor[9]. At the end, we get a floating point image for each family of stimulus (wedge and ring).

4.6 Results visualization

We can now visualize the images obtained through the functional processing and the statistical analysis described above. The first point to check is whether the angles values we found are properly located inside the cortex in the anatomical image with respect to a priori knowledge. We also check for the regularity of the angular values, as these angles should vary smoothly along the cortical surface.

[9]For more information about the SPM-Analyze format, see *http://www.mrc-cbu.cam.ac.uk/Imaging/analyze_fmt.html*

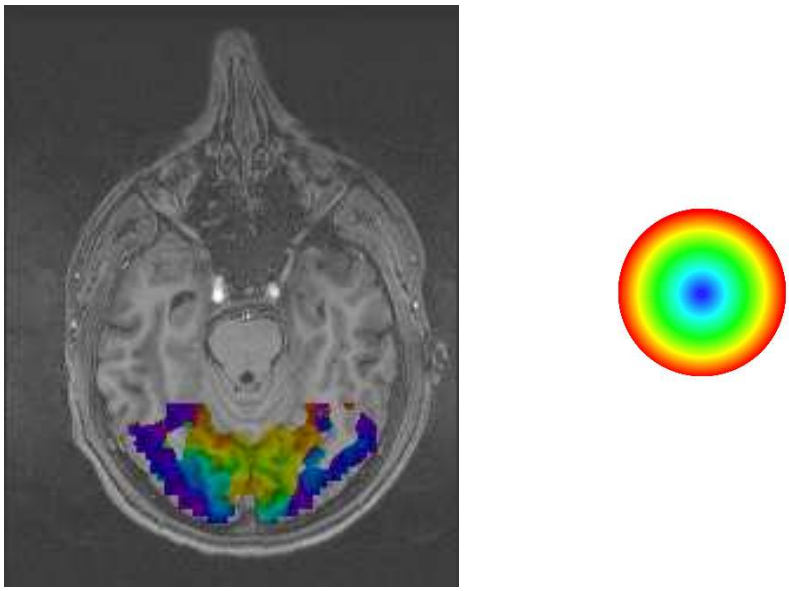

Figure 13: Angle values obtained for the ring stimulus, overlaid on the anatomical image. This map seems reasonably smooth along the cortical surface of the occipital lobe. The angles correponding to low excentricity values (fovea) are close to the occipital lobe, and we move further inside the brain as the excentricity increases, which is a global property of human retinotopy.

We have thus presented in this section the processings done on the functional data in order to extract the relevant informations to establish the retinotopy of a given subject.
A first observation of the resulting maps is even already possible at this step. However, the latter is not sufficient as it is laborious to follow the cortical surface in a 3D volume. In the next section, we briefly describe the Brainvisa software we use to extract a model of each hemisphere of the cortical surface, on which we project our angular maps.

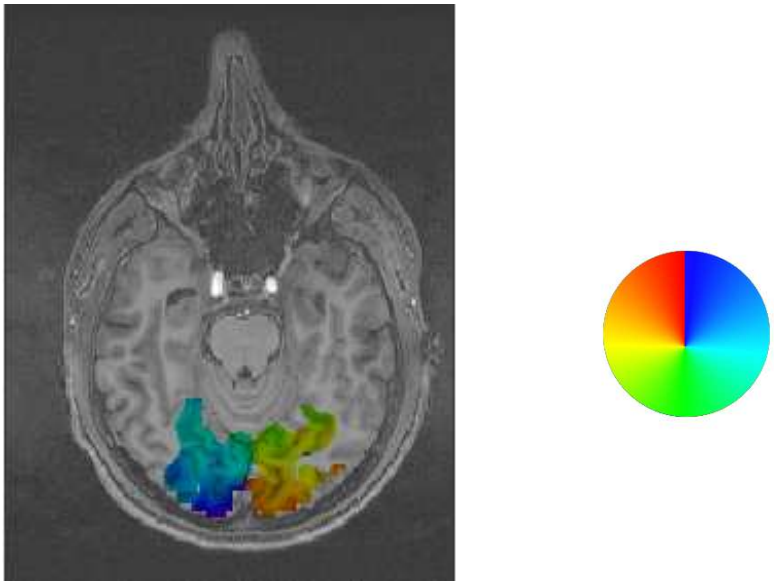

Figure 14: Angle values obtained for the wedge stimulus. This map also looks reasonably smooth along the cortical surface. We can easily check that the two visual hemifields project respectively to the contralateral hemisphere, a well-known property of human retinotopic maps of the first visual cortical areas.

5 Segmentation of the cortical surface

The aim of this section is to describe how to extract the cortical surface from the high resolution anatomical image. The cortex can indeed be considered as a surface, compounded of two connected components, one per hemisphere. Basically, we could see the cortex as a strongly folded sheet of tissue. It is thus a 2D surface embedded in 3D space. Ideally, finding this surface in the MR anatomical image comes down to determining the grey level value of the voxels corresponding to the cortex in the brain. Actually, many image distorsions prevent us from applying this straightforward procedure: (i) because of their relatively large size, the anatomical voxel often holds different tissues that are averaged -this is called the partial volume effect; (ii) depending on the sequence used, some tissues do not differentiate clearly in the image; (iii) heterogeneities in the coil also lead to a non-uniformity of the grey level in the image (bias), changing the grey level of a given tissue across the volume.
To perform this segmentation, we use the Brainvisa[10] software presented, e.g., in [3]. The first step of the algorithm we used is precisely meant to correct for the bias we mentioned above. It is then followed by a histogram analysis to detect the values for the different tissues we are interested in recovering the cortical surfaces, morphomathematical operations are then applied to the image to get a mask of each hemisphere, which are then segmented with regards to the grey and white matters, and finally the interface between the latter are tesselated. We further detail these steps in the next paragraphs.

5.1 Bias correction

If one observes a standard quality grey-level MR-anatomical brain image, it seems that each tissue is represented homogeneously. However, taking a closer look reveals that it is not the case, as we mentioned above: our visual system is used to correct for this kind of luminance variations. But a computer program is not able to compensate for these inhomogeneities; there is thus need to correct for this lack of uniformity, which is unfortunately not only linked to the scanner and the sequence (in which case measuring it once with an appropriate fantom would be sufficient to describe it) but also subject dependent.
To compute an intensity correction, the Brainvisa algorithm is based on a model of the observed intensity:

$$O(x) = I(x)F(x) + N(x)$$

where : I is the intrinsic intensity of the tissue,
F the spatial bias,
N the acquisition noise,
O the observed intensity.

The aim is to best estimate the spatial bias F, supposed to be spatially smooth which

[10]This free and open sources software, developped at the CEA-SHFJ, Orsay, France, can be found at http://brainvisa.info/index.html

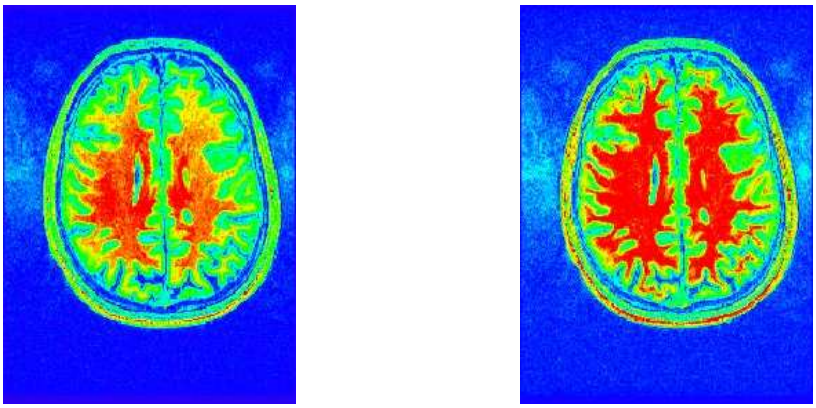

Figure 15: Bias correction of the anatomical image. The left image is the original one presented axially, the right one the result after the bias correction. The latter provides a more uniform grey-level value for each tissue. The colormap used here represents the white matter in red, showing the correction changes.

is reasonable with regard to the MR acquisition process. The algorithm is based on the minimisation of the following energy U:

$$U(F_C) = K_S S(F_C O) + K_R R(F_C) + K_M M(F_C O)$$

where $S(F_C O)$ is the resulting image entropy, $R(F_C)$ a function mesuring the spatial smoothness of the correction field F_C and $M(F_C O)$ a quadratic measure of the discrepancy between the original image mean and the corrected image mean. This latter term prevents the algorithm to converge to a null correction field. The constants K_S, K_R and K_M allow to weight each criterion of the energy. The optimization method implemented relies on a stochastic scheme. For a more detailed presentation of this method, see Mangin 2000 [13].
In order to judge the quality of the result, one compares visually the two images (original and corrected) and specially checks for the homogeneity of the white matter grey level (see figure 15).

5.2 Grey-level histogram analysis

We wish to evaluate automatically the grey levels of the different tissues we are interested in, here to distinguish mainly three classes: grey matter, white matter and the other brain tissues. Once again, the latter values differ strongly across scanners, MR sequences and subjects. The algorithm implemented in Brainvisa performs a grey level histogram analysis based on the scale-space theory (see for instance Koenderink 84,[12], Witkin 83 [31]) and relying on the two following invariant properties:
- There are three peaks in this histogram: one for the background, one for the grey matter

and one for the white matter, the order being always the latter;
- These peaks account for the largest amount of voxels.
We give an overview of the algorithm, detailed in [14]. Each tissue class should produce a specific mode in the image grey level histogram, and the modes order is constant across images. Starting from the study of scale space images derived from a mixture of two Gaussian distributions, one notices a structure linking the trajectories of the order i derivatives extrema to those of the order $i+1$ derivatives. This structure is always present independently of the Gaussian parameters, if we take a large enough order of derivatives, depending upon the case. With our MR images, the first two derivatives of the histogram are sufficient for the two modes of interest (white and grey matter). Assuming the modes to be relatively symmetric, the means are given by the minima of the second order derivatives and the standard deviations correspond to the maxima of the closest first derivatives. The algorithm thus uses these informations to group the trajectories using a notion of cascades and, after an automatic characterization of the sequence used to acquire the image (Inversion Recovery sequences show very distinct histograms for instance), the algorithm estimates the grey and white matter modes. Figure 16 illustrate the result of the scale space analysis of the histogram of one of our images.

5.3 Brain mask computing

A first binary image is computed by thresholding the original image with the values found in the previous step; this masks takes into account the voxels corresponding to the white and grey matter (mask=1) and remove the others voxels (mask=0). This is however insufficient, many other elements being kept (the eyes, meninx,...). A parameterized erosion process is simulated in order to whittle down this binary image. This erosion gives rise to different connected components, from which the largest one is kept as a brain seed. A dilation process is applied to this seed to recover the brain. Figure 17 illustates these steps. As for the bias correction, the resulting mask should be checked visually onto the original image. For our retinotopic experiments, care was mainly pointed on the occipital lobes (at the back of the brain) where the first retinotopic cortical visual areas are located. As one can easily notice in figure 18 on the coronal and sagittal views, the cerebellum is included in the mask. An algorithm, based on Chamfer distances and computing a Voronoi graph, allows to classify the mask into three distinct parts: the cerebellum, the left hemisphere and the right hemisphere. Separating the two hemispheres is particularly important for our studies, as the visual areas are mainly located on the medial sides (between the two parts). The final result is shown in figure 19.

5.4 Grey matter/white matter classification

The last step before building the meshes is to compute, using the mask and the histogram analysis, a classification of the tissues in each hemisphere mask. The result does not only come from a mere thresholding but includes a markovian regularization: a voxel with inter-

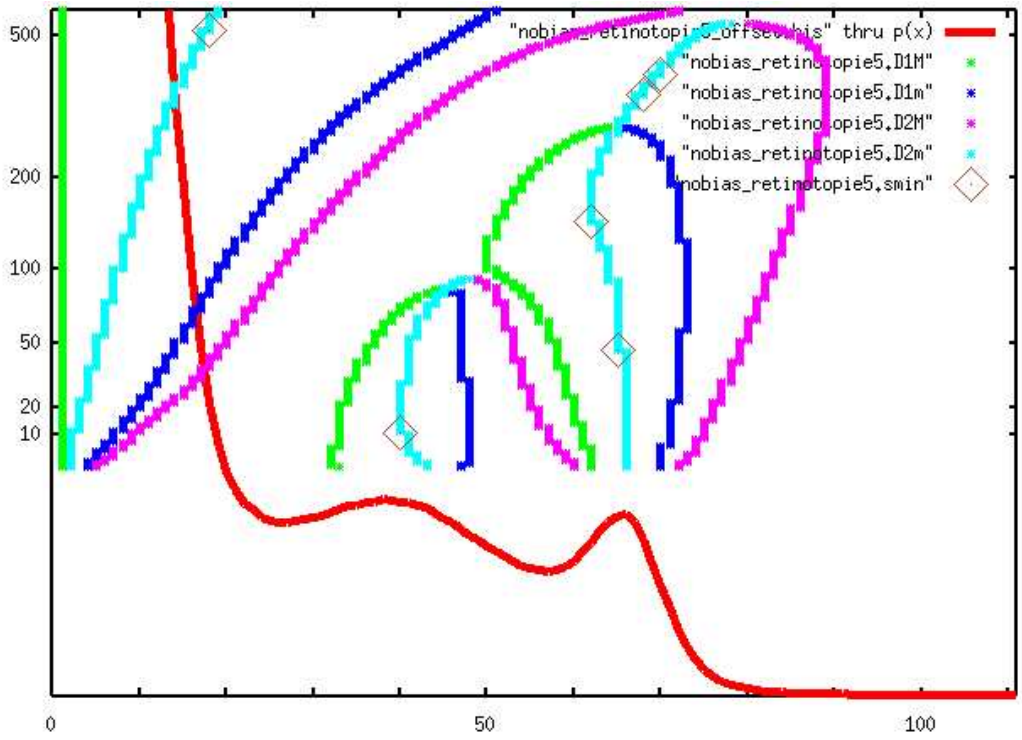

Figure 16: Histogram analysis based on the scale space theory. The grey levels are shown horizontally and the scales vertically (on a log-scale). The red curve is the grey level histogram of the image, the caption of the figure indicates the colors for the trajectories of the minima (m) and the maxima (M) of the first two derivatives.

mediate grey level is assigned preferentially to the majoritary class of voxels surrounding it. The result is shown in figure 20.

5.5 Cortical surfaces extraction and functional maps projection

From the mask computed previously, we extract two cortical surfaces in 3D space (one per hemisphere), and we then project our angular maps onto these two surfaces.

5.5.1 Cortical surface model

The cortical surface of a given hemisphere is modeled using the grey matter/white matter interface. The latter is detected on the segmented mask presented above during the grey matter/white matter classification in each hemisphere. The surface is further constrained

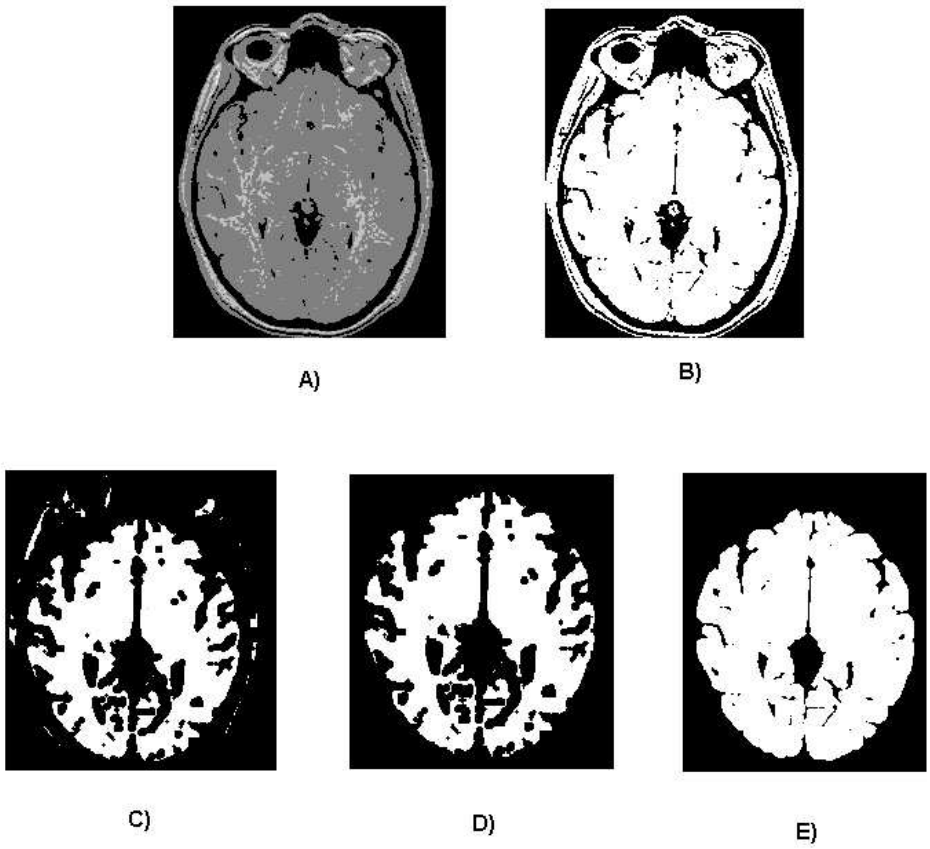

Figure 17: Illustration of the different steps for the brain mask computation. A is the original anatomical image. B is the thresholded image: the thresholds were extracted from the histogram analysis. C is the result after the first erosion on B, D the largest connected component in C and E the final brain mask after dilation.

to have a spherical topology. A close to standard marching cube algorithm is used to compute a triangular spherical mesh. Finally, a decimation is applied to the mesh, including a smoothing to avoid artefacts due to the underlying discretization. The decimation strength depends on the trade-off between the final expected quality of the mesh with respect to the segmentation and the mesh size.

The top-left image in figure 21 ($i = 0$) shows the result of the meshing for a given hemisphere.

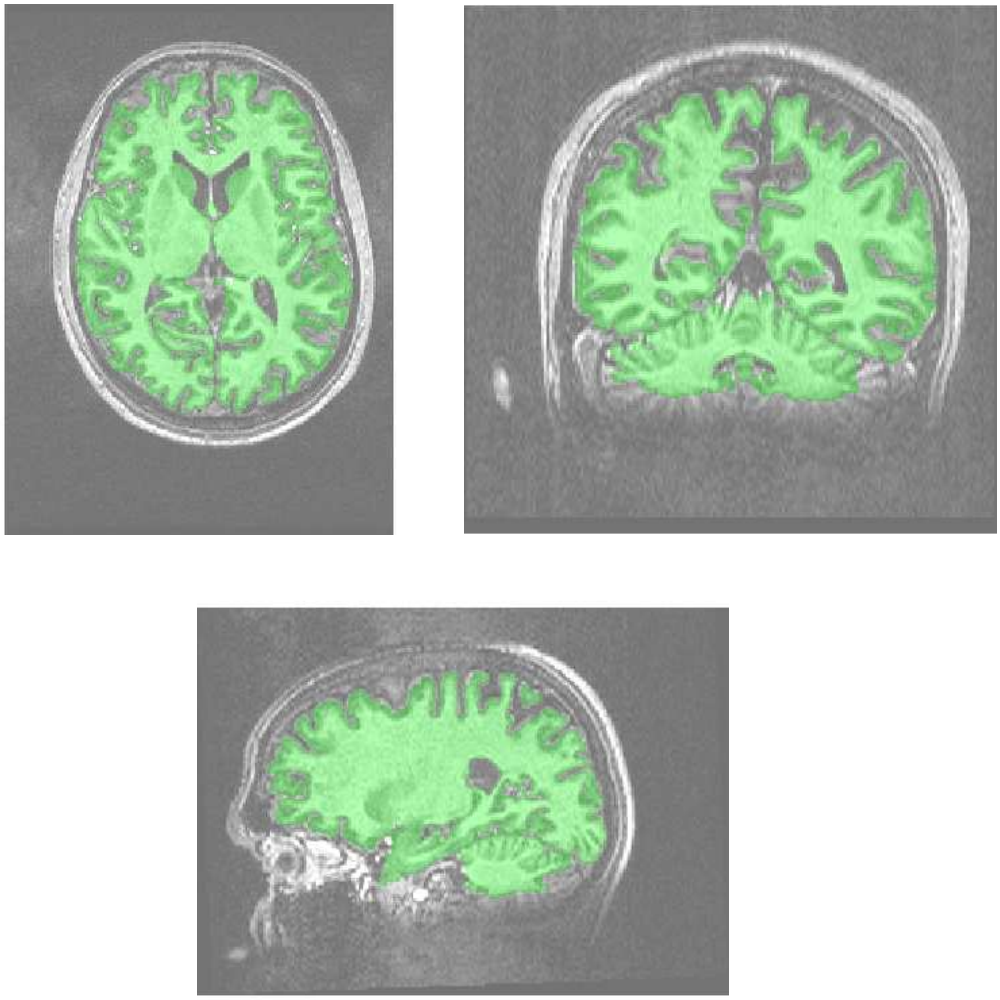

Figure 18: Visual check of the mask quality, along three directions: axial (top-left), coronal (top-right) et sagittal (bottom). We check that the mask correctly fits the sulci and the gyri, especially in the occipital part of the brain we are mostly interested in (location of the first visual areas)

Figure 19: Brain mask, separating the two hemispheres and the cerebellum

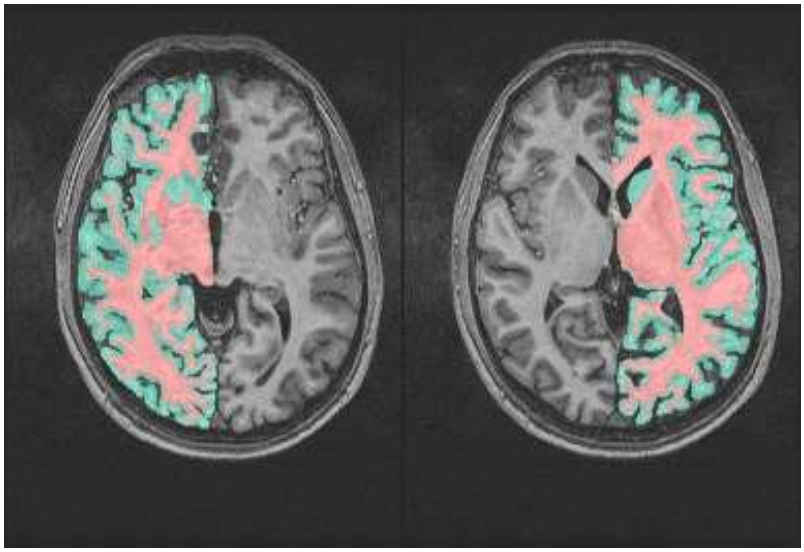

Figure 20: Grey matter/White matter classification in the two hemispheres.

5.5.2 Functional data projection

This stage consists in the attribution of a functional (scalar) value to each vertex of the mesh. Different methods can be used:

- The voxel value that contains the current vertex.
- Move in 3D along the normal to insure being inside the cortex, our surface being an interface with the white matter).
- Average the values from different voxels in a sphere centered at the current vertex.
- Average the values from the voxels crossed by the surface normal defined at the current vertex along a given distance supposed to be the cortical surface thickness.

The result changes with the method used. We generally prefer the last because it is meaningful with respect to the columnar organization of the cortex (the cortical columns are indeed orthogonal to the surface, thus locally oriented along its normal) and empirically leading to more complete maps. The sub-method used for the averaging also plays a role. We generally used a corrected mean to exclude voxels out of our statistical mask whose value is set beyond $[-\pi, \pi]$ (typically at -3.2).
All the methods mentioned are implemented in the Anatomist visualization software we used.

5.6 Cortical surface inflating

The cortical surface shows a complex geometry, mainly through its highly folded configuration, making the results visualization particularly awkward inside the sulci. Two different techniques, based on unfolding the cortical surface, are usually used to improve the visualization: flattening it or inflating it. In both cases however, distances and/or angular distorsions are unavoidable.
In this study, we used the second method, inflating the cortical surface of each cerebral hemisphere. The algorithm relies on an energy minimization allowing to compute an inflating force at each vertex of the mesh. This force is made of three components:
- a strictly speaking inflating component, along the current vertex normal,
- an "elastic" component, trying to maintain the distances between neighboring nodes,
- a smoothing component, moving each node toward its neighboring vertices.

The inflating is the result of a trade-off between these three components. The texture mapping applied to the original mesh (presented above) is only done once, as the evolution of the mesh keeps the same vertices neighbors, thus cancelling the need for another projection on the resulting mesh. The algorithm further allows to save images of the process during the energy minimization, thus allowing an easy tracking of the sulci and gyri along the process. The global result is satisfying, although perfectible notably when the curvature is locally large. Figure 21 presents some images of a left cortical surface at different stages of the inflating process.

We have thus presented the different steps allowing an efficient visualization of the functional processing results on the cortical surface. We can now move forward to the final step of the retinotopic mapping, that is exploit the data to (i) study the retinotopic maps of a given subject, (ii) delineate the primary cortical visual areas.

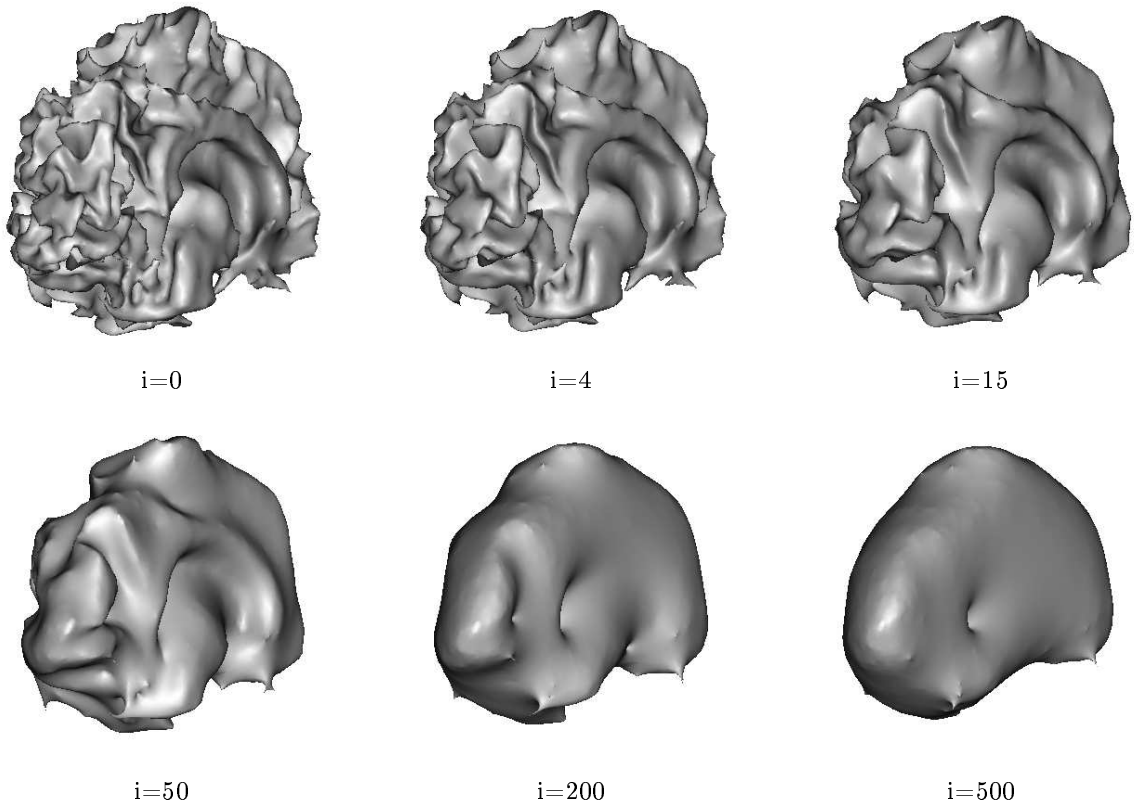

Figure 21: Different stages of the inflating algorithm on a given left cortical hemisphere, i indicates the iteration step.

6 Results

We are now able to visualize our angular maps projected on a mesh of the cortical surface and to inflate the latter to avoid the problems due to the folds.
In this chapter, we first show the qualitative aspects of our retinotopic maps, comparing our results to the literature. Our angular maps resulting from different stimuli, show a good reproducibility and provide the optimal stimulation to use with respect to different parameters. Lastly, we explain the method used to delineate the visual areas based on retinotopic criteria.

6.1 Retinotopic maps

Thanks to the extraction of the angle maps from our two families of stimuli, the ring and the wedge, on one hand (see section 4) and the construction of models of the cortex geometry on the other hand (see section 5), we are now able to render the eccentricity and the polar angle maps on the subject's cortical surfaces respectively, and to further infer some general information regarding the organization of human occipital retinotopic areas.

6.1.1 Eccentricity maps

General results The ring stimulus is used to get the phase-encoded eccentricity map, mapping the cortical responses to a ring located at various eccentricities. Our stimulus extends up to a maximum of 16.5 degrees.
As a general qualitative result, we find, for every subject tested, the classical pattern in which the foveal representations lie in the occipital poles and as eccentricity increases, the representations appear further anterior and medial.
In [27], Wade etal. also reported an isolated foveal representation anteriorly to the V1/V2/V3 areas. We confirm the presence of this foveal patch in our maps for every hemispheres analysed. Figure 22 shows an eccentricity map for one hemisphere.

Foveal sensitivity The eccentricity maps on the cortical surface are smooth and qualitatively match what we expected to see from other studies.
However, the extreme occipital pole is hardly fully covered of angular values, whereas we can expect here a foveal representation. We wondered if the periodic stimulation paradigm we use was sensitive enough to foveal stimulus position. To answer this question, we used a classical block design to contrast a 5 degrees eccentricity stimulation with a uniform grey field fixation (see figure 23). Each condition was presented 10 times, each block lasting 8 TR (or 16,888 s).

The analysis is performed classically with a linear regression on the box car function representing the stimulation (1 during foveal presentation, 0 otherwise) convoluted with a classical hemodynamic response model from SPM. No spatial smoothing was performed on the data, to prevent any blurring effect. We present in figure 24 the comparison between the t-map drawn from this block design experiment and the angular values computed from

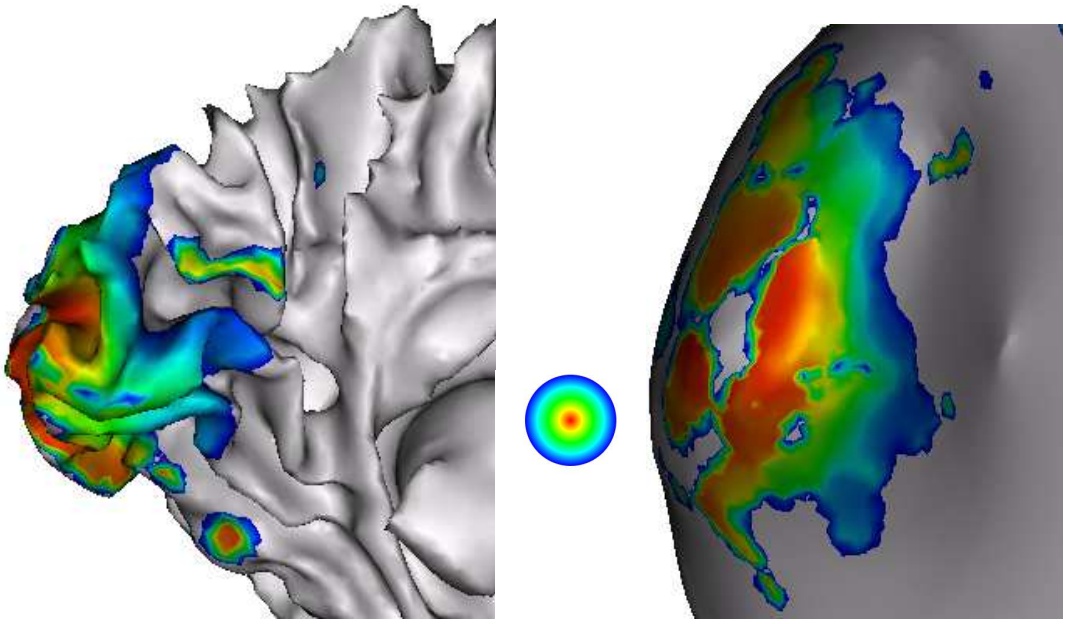

Figure 22: Example of the eccentricity map in a medial view of a left occipital lobe. The left figure shows the original surface and the right one an inflated view. We can clearly see the isolated ventral foveal activation reported by Wade etal. [27], located beyond hV4 if we also use the polar angle map to segment the areas (see below). The color gradient going to blue at the border of the map does not correspond to an angular representation but is actually an Open GL interpolation bug that cannot be changed under the current version of the Brainvisa plateform.

4 cycles (contracting and expansing) of the ring stimulus. We compared directly the results in slices of the 3D volume to avoid any problem that could arise from the cortical surface extraction or the projection of the functional data onto it. The comparison is presented here for a single axial slice, but the result is qualitatively equivalent for any slice of the volume: there is a global overlap between any value in the eccentricity map coding for a foveal ring position and supra-threshold t-values from the block design foveal stimulation. This is in particular the case in the ventral foveal representation, beyond V4, mentioned above. At the very pole of the occipital lobe, we do not find any significant t-value, as we could expect from the eccentricity map. This lack of signal at this precise anatomical location is also often present in the litterature's figures of eccentricity maps, though this point is generally not discussed. It is nonetheless quickly discussed in a footnote in [17]. One reason could come from small eye movements, making the signal very low in the macula; a lack of power in the

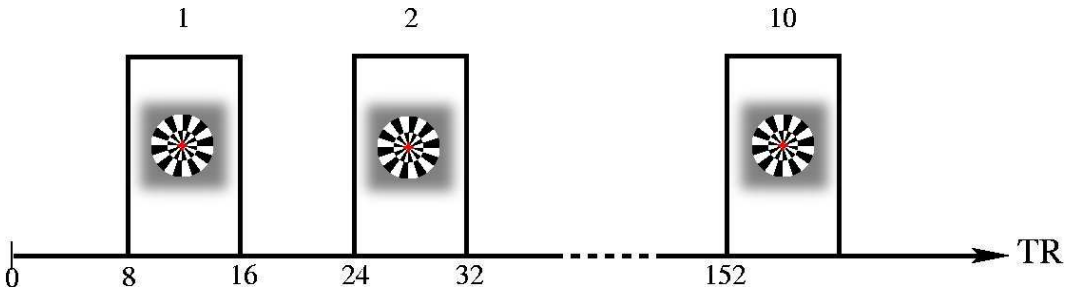

Figure 23: The block design used to map the foveal representations in the occipital cortex. Blocks between two foveal stimulation blocks, the null conditions are uniform mid-grey field with the red fixation cross.

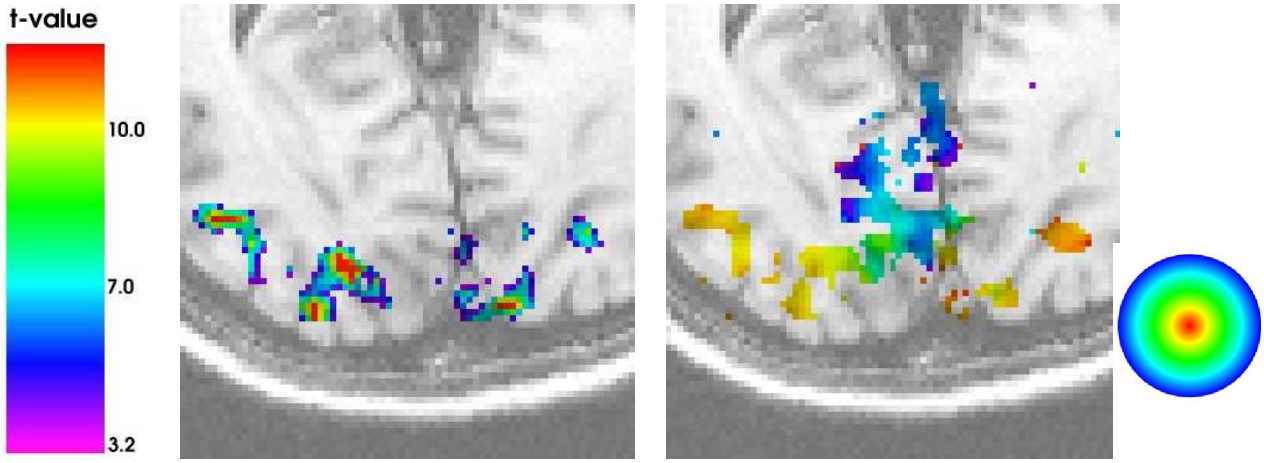

(A) Block foveal (B) Ring (4 cycles)

Figure 24: Comparison between (A) the t-map, contrasting foveal stimulation blocks versus uniform grey field fixation blocks (3.2 is the t-value of p=0.001) and (B) the eccentricity map derived from the 4 cycles ring stimulus, in an axial slice. The t values above the statistical threshold in (A) completely match the low angular values in (B).

measurements and the different analysis processes could also explain this missing "center of gaze" representation.

6.1.2 Polar angle maps

General results Stimulating a subject using the wedge stimulus allows to get his polar angle map, mapping the cortical activity implied by a cone located at different position around the center of gaze. From previous neurophysiological studies, it appears that the boundaries of early retinotopically organised visual areas are defined by reversals in the representation of the polar angle. This stimulus is thus sufficient to segment retinotopic visual areas.
As for the eccentricity maps, the general pattern of representation of the visual field on the cortical surface is smooth, according to the definition of the retinotopy. From the literature agreements, we can expect the following for one hemisphere:
- V1-also called the "striate" cortex with respect to its markedly laminated anatomy and its 11 layers (rather than the customary 6 in other areas) and by opposition with the next "extrastriate" areas- has a complete contralateral hemifield representation, covering the calcarine sulcus. The horizontal meridian lies in the fundus of the latter and the representation smoothly changes to the superior vertical meridian in the ventral lip of the calcarine sulcus and to the lower vertical meridian in the dorsal lip of the calcarine sulcus respectively. These vertical meridians define the borders of V1 with the two distinct parts of V2. The representation in V1 is qualified of mirror, as the visual field is projected on the cortical surface as if seen through a mirror (see section 2.2).
- V2 is divided into two distinct quarter-field representations, the upper contralateral quadrant being situated ventrally to V1 (V2v for V2 *ventral*) and the lower contralateral quadrant dorsally (V2d for V2*dorsal*). Unlike V1, the representation in V2 is non-mirror. In other words, the polar angle gradient along the surface is reversed with respect to V1. The borders of V2v and V2d with respectively V3v and V3d are defined along the horizontal meridian representations.
- V3, akin to V2, is split into two quadrants. V3d follows V2d as one moves dorsally and shows another lower quarter-field representation; V3v, also called VP for Ventral-Posterior because it was suspected to be distinct from V3d in monkeys studies, follows ventrally V2v and shows an upper visual field quadrant. We chose to call this portion of the cortex V3v instead of VP, as this separation between the two aim at being less and less supported in the monkey litterature and as no evidence was presented to distinguish them in humans (for a more complete discussion, see Zeki's paper about "improbable areas" [34]). The representation in both parts of V3 is reversed with respect to V2, thus mirror like V1.
- V3A, located dorsally to V3d, shows a complete contralateral hemifield non-mirror representation.
Figure 25 clearly shows the patterns detailed above and generally found in human fMRI retinotopic papers.

Beyond the "great agreement zone" Beyond V3A dorsally and V3v ventrally, maps and conclusions are getting less consensual in the human fMRI retinotopic mapping community.
In the dorsal occipital region, another quarterfield representation was reported in Van Oos-

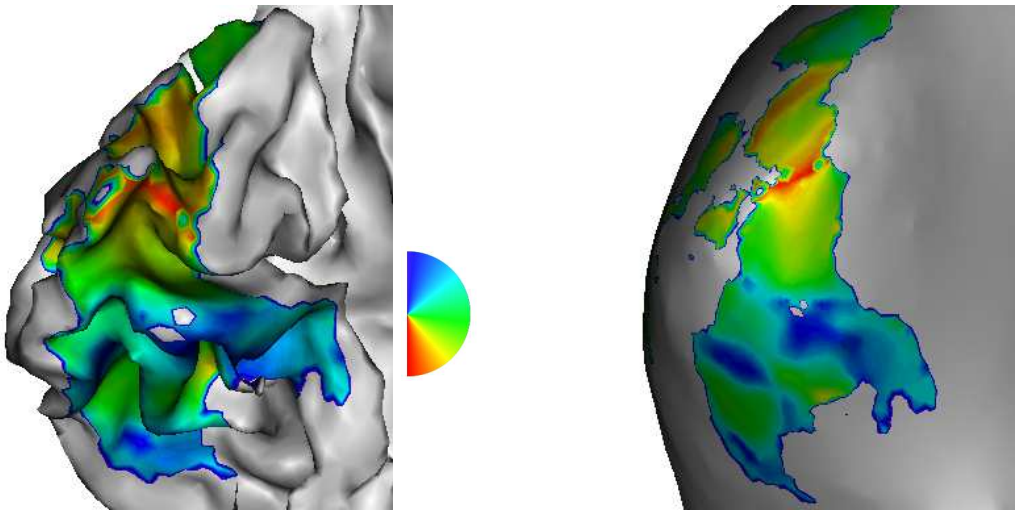

Figure 25: Polar angle map on a left hemisphere. We find the general angular values pattern described in the text and reported in the litterature.

tende et al. [26] and later named KO, or V3B in Smith et al. [20], whereas a complete hemifield representation was afterwards reported by Press et al. in [16] at the same location (following Smith and colleagues, they called it V3B). Tootell et al. also reported in [23] and [22] another area next to the V3A/V3B region, called V7 and supporting an upper quarterfield representation. Yet, Press et al. later report in [16] a complete hemifield representation in this area V7.
Our results in this portion of the cortical surface are less reproducible from subject to subject and often lack signal, probably because we reach the accuracy of our method which performs too fast retinotopic maps aquisition to provide enough signal (only 8 complete cycles for each rotation direction of the wedge, without any additional averaging of runs). These issues should be resolved with a more sensitive data acquisition (for instance using a surface coil), with more cycles in the stimulus presentation or an averaging of signals across different acquisition sessions and maybe with further improvements in the data processings. Moving ventrally beyond V3v, we also find some retinotopic signal, but the visual field representation and the labelling is once again not consensual here. Hadjikhani et al. reported in a Nature article [10] a quarterfield representation, labelled V4v, followed by a complete representation they called V8 (supposed to be a color sensitive area). But the authors only present one dataset with a V8 fovea, whereas later publications from this group (see for instance Tootell and Hadjikhani, Cerebral Cortex, 2001 [25]) show retinotopic maps not always consistent with this result. In [27], Wade et al. reported a complete hemifield representation sharing a vertical meridian with V3v.

According to our data, our conclusions are closer to those from Wandell's laboratory, as shown in figure 26. The V8 assumption seems invalidated by the absence of foveal representation for each polar angle values in this portion of cortex beyond V3v.
But once again, more reliable signal is required in this ventral region of the occipital cortex to draw a solid conclusion.

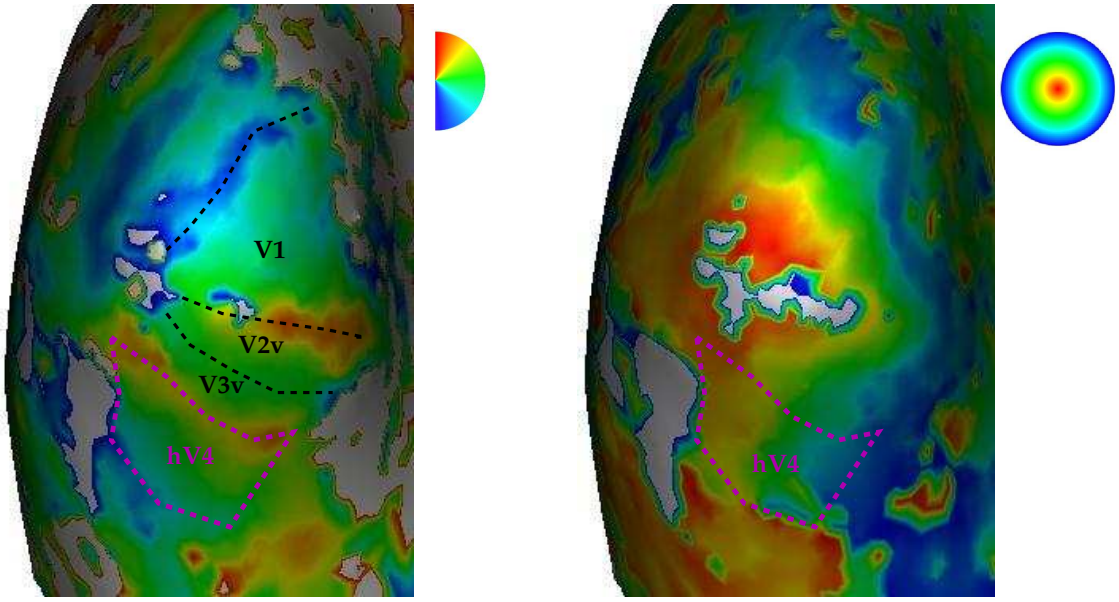

Figure 26: Example of hV4 polar angle and eccentricity maps. These results seem consistent with a complete hemifield representation beyond V3v.

Wedge stimulation optimization As we mentioned in paragraph 3.3.2, we tested different conditions for the wedge stimulus in order to optimize our stimulation process. Following Warnking [29] and Slotnik and Yantis [19], we tried a bifield wedge, for two main reasons:
- the stimulus being symmetrical with respect to the fixation point, the subject would be helped maintaining its gaze in the center of the display,
- the stimulation could run twice quicker.
Besides, a three wedges (or more) stimulus would lead to more difficulties with the signal phase interpretation. Indeed, the analysis remains globally the same, but the results show a phase ambiguity: a given value of the phase of the BOLD response corresponds to two locations in the visual field. However, the prior knowledge about retinotopic maps shows that this ambiguity only appears with the vertical position, other positions being uniquely defined on each hemifield, thus in each hemisphere (see paragraph 2.2). The vertical position

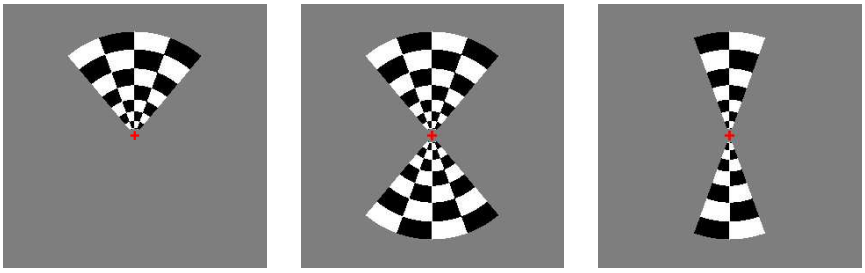

"Unifield" Wedge "bifield" 80° Wedge "bifield" 40° Wedge

Figure 27: The differents wedge stimuli tested.

can be disambiguated taking into account the expected local smoothness of the maps.

We first compared the final maps obtained with the classical 80 degrees unifield wedge, a 40 degrees and a 80 degrees bifield wedge as shown in figure 27. Figure 28 shows the results we obtained with these bifield wedge stimulation with respect to the unifield wedge on a representative hemisphere. The rotation velocity for the bifield wedge was twice that of the unifield wedge. This is probably the explanation of the convergent results we obtained for 3 different subjects, where the bifield stimuli give less comprehensive maps than the unifield. Indeed, if the stimulation frequency is too high, the low pass filter of the hemodynamic response removes these high frequencies, including the fundamental stimulation frequency, in many voxels. Besides, the higher quality achieved with the 40 degrees bifield wedge than with the 80 degrees also comes from the hemodynamic filtering, preventing the signal to return to its baseline between two stimulations. This phenomenon is supposed to occur twice as much with the 80 degrees wedge than with the 40 degrees.

To strictly isolate the bifield versus the unifield wedge comparison, we did another experiment on 3 different subjects, using the same rotation velocity for each stimulus. Figure 29 shows the result for such a comparison on a representative hemisphere. Maps qualitatively look much closer to each other in this comparison than in the previous one, but the amount of supra-threshold voxels is still higher for the unifield stimulus. The reason could come from the eye movements of the subject, twice more likely to lead to unexpected stimulation, considered as noise, thus modifying the signal time course, than with the unifield stimulus. However, as we are not yet able to measure eye movements during the experiments, we can not quantitatively confirm this assumption.

As a conclusion for this multiple comparisons with the wedge stimulus, the unifield wedge with a rotation frequency of 1/38 Hz was kept for its higher accuracy.

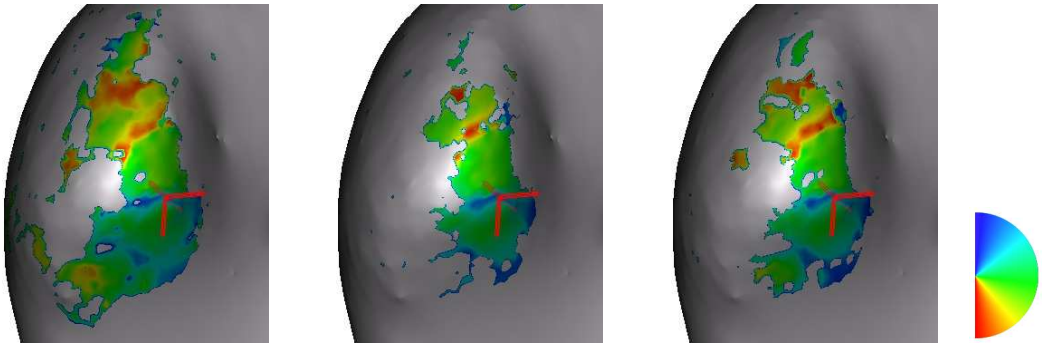

"Unifield" Wedge "bifield" 80° Wedge "bifield" 40° Wedge

Figure 28: Comparison of polar angle maps projected on an inflated left hemisphere with respect to different stimulations. The unifield stimulus clearly leads to more signal, thus angular values, than the bifields, rotating at twice the unifield wedge velocity.

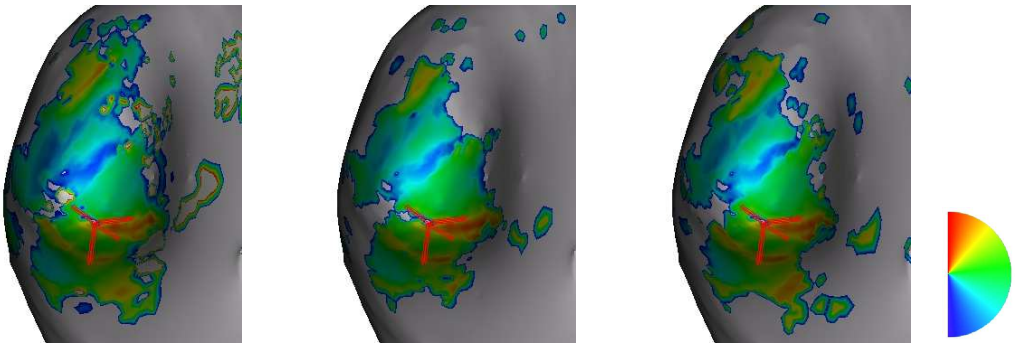

"Unifield" Wedge "bifield" 80° Wedge "bifield" 40° Wedge

Figure 29: Comparison of polar angle maps projected on an inflated left hemisphere with respect to different stimulations. The unifield stimulus leads to more activations than the bifields, however rotating at the same velocity.

6.2 Reproducibility

Beyond the confrontation of our maps with the results from other labs, one way to assess the robustness of our retinotopic mapping procedure is to study its reproducibility, inter-subjects but also intra-subject.

6.2.1 Inter-subjects reproducibility

As already discussed in paragraphs 6.1.1 and 6.1.2, our maps are in agreement across subjects, as we globally find the same patterns of angular values representations, at least in the portion containing V1, V2, V3 and V3A.

6.2.2 Intra-subject reproducibility

Intra-session The stimulus optimization we have detailed in the previous paragraph allows us to check for the reproducibility of the maps in a given subject within the same scanning sesssion. Figures 28 and 29 illustrate this intra-session reproducibility of a given subject, using different stimulus parameters. The red crosses are linked for each image, showing the high quality alignement of area borders (here the lower boundary of V1) thus revealed. The differences in the maps result only in a lack of significant signal at some voxels, to be mainly linked with the changes in stimulation as discussed in the previous paragraph.

Inter-session The reproducibility of the maps derived from a given subject through different scanning sessions was also assessed for different subjects. The results for one of them are shown in figure 30. The different maps are computed independently for each session. The realignement between different structural T1 images acquired at each session is done using the standard SPM coregistration algorithm, registering session N ($N \geq 2$) anatomical scan on the corresponding data for session 1. The transformation found is then applied to the angular maps computed with the data from the sessions 2,3, etc., and all the results are displayed on the inflated mesh of the left grey matter-white matter interface. These results show the good intra-subject and inter-session reproducibility of our processing chain, even using a basic registration procedure. Indeed, even if the maps do not completely overlap, the angular patterns are equivalent and the areas segmentation that we would get from these maps are equivalent. This inter-session reproducibility was systematically found.

6.3 Area delineation

Beyond the study of the retinotopic pattern on the cortical surface, this retinotopic mapping method allows one to delineate the different retinotopic areas revealed. We first present the Visual Field Sign method we tried and then quickly describe a manual procedure we can

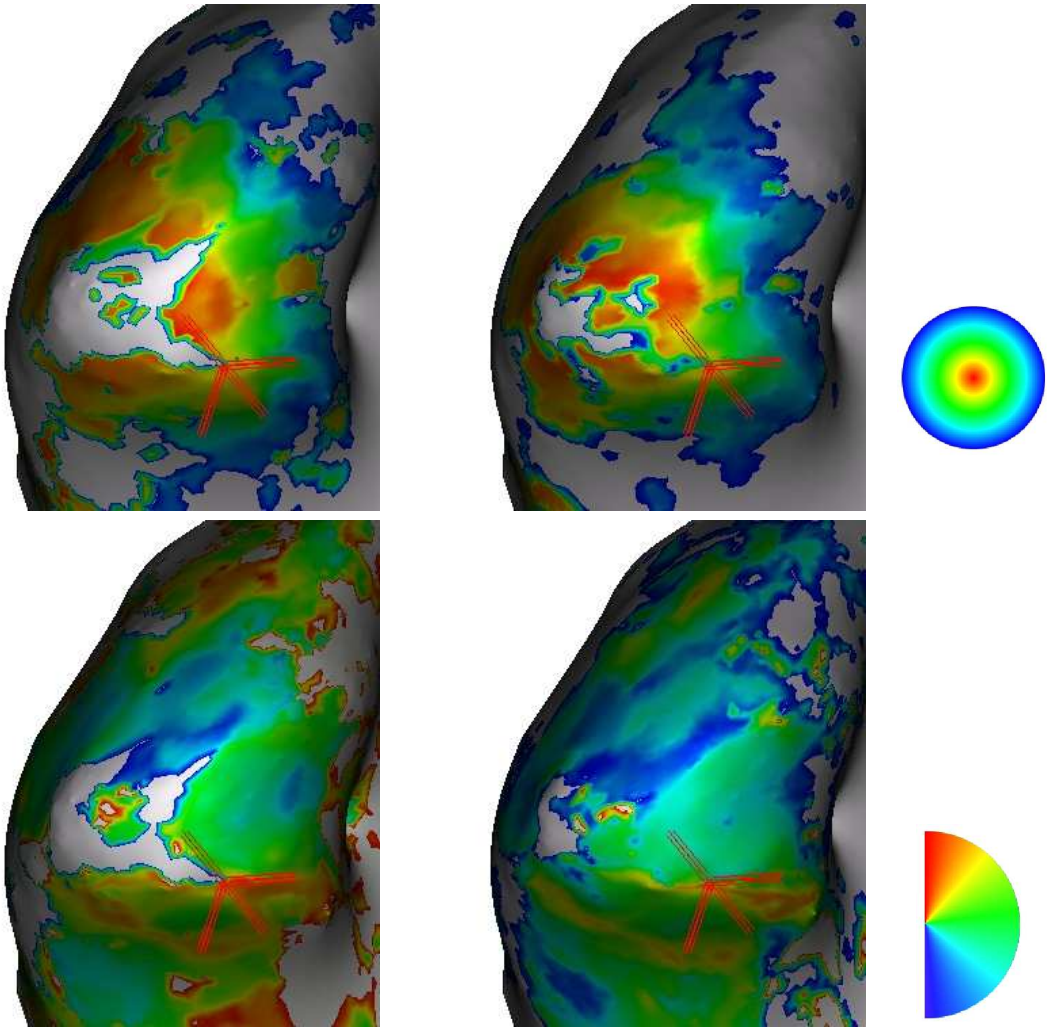

Figure 30: Intra-subject inter-session maps reproducibility. The maps from session 2 were realigned in session 1 coordinate system using the anatomical images coregistration transformation. The maps are qualitatively identical, showing the high reproducibility of the whole procedure. The main differences are "holes" in the maps due to a loss of signal to noise ratio in some voxels. The red crosses show a linked position in each image, located on a point of V1 foveal and upper vertical representations.

use to delineate properly the visual areas.

6.3.1 Visual Field Sign maps

In [18], Sereno et al. introduced an automatic method combining the excentricity and polar angle maps to construct the Visual Field Sign (VFS) map, allowing a direct delineation of the retinotopic cortical areas from electro-physiological data. The technique was then successfully applied to fMRI retinotopic maps in [17] and [29], and implemented in a volumetric fashion in Dumoulin et al. [6].

The Visual Field Sign is computed from the gradients of the excentricity (noted $\nabla\rho$) and the polar angle (noted $\nabla\theta$) maps computed on the cortical surface. The formula is:

$$VFS = sign(det(\partial\psi))$$

where ψ is the function mapping, for each point on the cortical surface, its position in the visual field, as shown in figure 31. The detailed formula is thus:

$$VFS = sign(det(\nabla\rho, \nabla\theta, N))$$

where N is the exterior normal to the cortical surface.
Taking into account the retinotopic properties of the visual cortex, this sign will change between two neighboring areas, allowing us to easily delineate them.
The gradient directions of both functions ρ and θ (defined on the cortical surface) are estimated at each vertex of the underlying mesh with a least square method, using the neighborhood information of the current vertice. Formally, we look for the vector V minimizing:

$$\|\delta F - V\delta X\|$$

- F is the function ρ or θ, δF is a local variation of F,
- δX is a local variation of the cortical surface coordinates.

By definition of the gradient :

$$\begin{aligned} & dF = \nabla F dX \\ \Rightarrow \quad & dF^T = dX^T \nabla F^T \\ \Rightarrow \quad & \nabla F^T = \left(dX dX^T\right)^{-1} dX dF^T \end{aligned}$$

This computation is done at each vertex of the mesh, directly on the cortical surface, modelling it locally as a plane orthogonal to the normal N. We made this computation on the inflated surface, avoiding problems with locally high values of the curvature (where the local plane approximation of the surface would not be valid anymore).
We first encountered a problem with this computation, many gradients being close to zero.

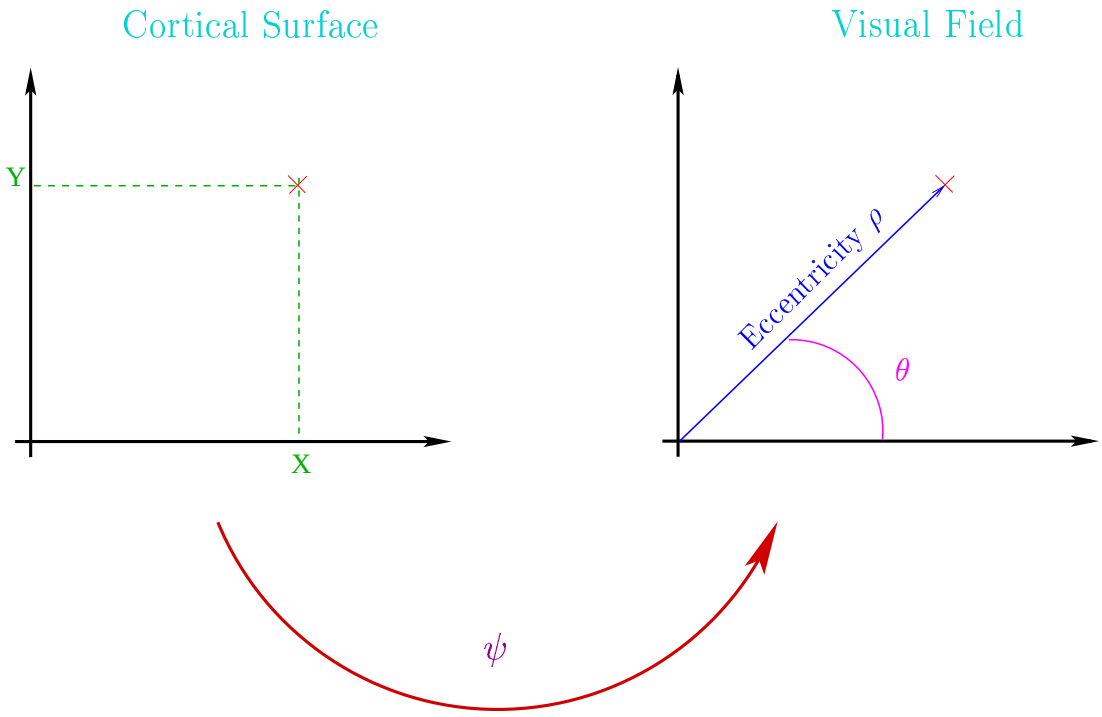

Figure 31: Schematic representation of the ψ function, linking points defined on the cortical surface to the corresponding prefered position - supposed to be the center of an ideal voxel's receptive field - in the visual field.

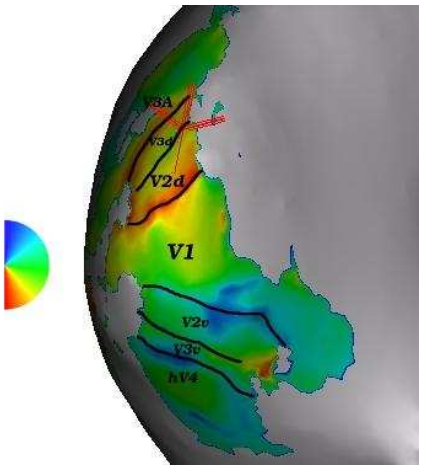

A) Polar angle map

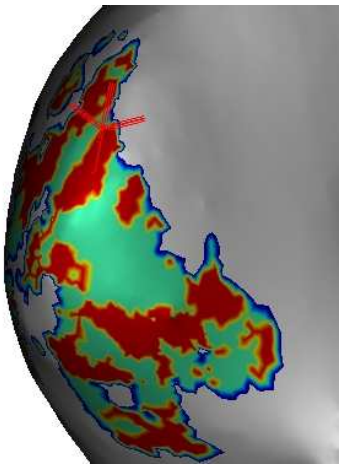

B) VFS map

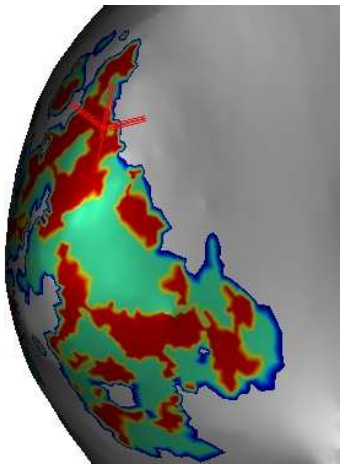

C) VFS map after angular maps smoothing

Figure 32: Visual Field Sign maps (see text). A) shows a polar angle map projected on an inflated left occipital cortex. The area boundaries were drawn by hand, based on the angular gradients. Images B) and C) represent respectively the results of the visual field sign computing, based on the original polar angle and eccentricity maps and after a surface-based smoothing of the angular maps with a gaussian kernel ($\sigma = 3mm$) in C). Red (green) color indicates a non-mirror (mirror) local representation. The smoothing does not globally improve the global result; the red cross even shows a position where the original VFS (left) performed better.

Indeed, the cortical mesh is much more precise than the original volume of the functional data. We have thus oversampled our original angular maps on the mesh, often giving rise to close to null variations between two neighboring vertices. To solve this problem, we considered a higher order neighborhood. For instance, the 2nd order neighborhood of a vertice v is made of the neighbors of the neighbors of v, without its first order neighborhood and v itself. Depending on the degree of the mesh precision (increasing the latter globally decreases the distance between nieghboring vertices), it was found to be useful to use a third or even higher order neighborhood to have a more reliable estimation of these gradients. This indeed solved the problem that led to null gradients at many vertices. However, a second problem remained: the VFS map obtained was still noisy with respect to the delineation we wished to get. We therefore tried to smooth the ring and wedge angular maps on the cortical surface using an appropriate surface-constrained smoothing method as described in [21], which was supposed to avoid this problem. It actually did not enhance sufficiently the results (see figure 32).

Looking closer at the data on the surface, it appeared that our angular maps were not as regular as they were supposed to with respect to electrophysiological data, explaining the problems we encountered with this visual field sign computation. Besides, oral communications with other laboratories applying the retinotopic mapping techniques and trying the VFS led us to the conclusion that this method is not robust enough for fast acquired retinotopic maps. Let us recall that our technique allows the acquisition of these maps (eccentricity and polar angle) with 15 minutes of functional scans, which is considerably less than what is usually reported in the litterature (cf [33] for a comparison).
Finally, looking closely at the results shown in the literature using the VFS computation, it often reveals the same noisiness in the VFS maps. This review led us to look for an alternative way to define our retinotopic areas.

6.3.2 Manual area delineation

In order to get a correct delineation of our visual retinotopic areas, we can use a manual area definition, mainly based on the polar angle map of the subject. Indeed, this map gives the information of angle reversion needed to delineate properly connex areas.
This method allows us to correct for the noise found in our VFS map -which can nonetheless be used as a starting point- and could also be used to completely delineate the retinotopic areas solely based on the polar angle values, allowing an even faster functional scanning session if needed.
We adapted the SUMA[11] software to our needs, allowing to draw on the inflated cortical surface and to save the 3D vertices coordinates from the original (non inflated) surface. This adaptation mainly involved data formats and coordinates system conversion between the different softwares we use. We then perform a "back-projection" consisting in the attribution, for each vertex, of a subset of voxels in the original volume, according to the

[11] Software, developped by Saad and Cox at the NIMH, NIH; documentation and binaries are freely available at http://afni.nimh.nih.gov/sscc/staff/ziad/SUMA/SUMA_doc.htm

projection technique used to map the functional values on the cortical surface. We typically use an integration (i.e. an averaging) of the values met at different voxels from the vertice considered (lying on the grey matter/white matter interface) to a certain distance along the local normal to the surface; this distance is supposed to match the cortex thickness, typically 3mm. This technique allows us to derive volumic Regions Of Interest (ROIs) from surface-based defined regions, for instance the voxels subset supposed to represent V1. These ROIs can then be used for any further experiment characterizing more precisely these retinotopic visual areas.

We are able to delineate retinotopic areas of any given subject, using 15 minutes functional scans and an anatomical image. This however requires some time consuming and probably somewhat less reproducible manual editing than an automatic delineation. We might further try other approaches like [5], using a model for each angle map and warping these models onto the actual measurements, or [6], allowing a volumetric visual field sign computation (even if the resulting VFS maps of the latter technique are not as smooth as expected).

***

The retinotopic maps we obtained are globally in agreement with the related literature and our results confirm some cutting edge questions in the field, as the presence of a ventral fovea representation beyond V3v.
Beyond this mapping aspect, we can derive from these retinotopic maps ROIs that can be used in further experiments exploring the human cortical visual system. As our acquisitions are fast enough, other functional scans can be performed within the same scanning session, the retinotopic mapping allowing a functional definition of ROIs.

7 Conclusion

Based on methods published in the literature, we have detailed our method to obtain a human individual retinotopic map of the occipital cortex using fMRI, from the generation of the stimuli to the visualization of the results. The acquisition time is below what is generally described and the resulting maps are consistent with those published. These results furthermore show a reliable reproducibility, across and among subjects.

This method allows us to (i) study the retinotopic representations in the human occipital cortex, which could lead to define new retinotopic areas in this region of the visual cortex and (ii) define Regions Of Interest (ROIs) that can be used for further study and functional characterization of the low level visual areas thus revealed.

However, our technique also shows its limits to deepen the knowledge on retinotopic representations beyond the consensual areas around the calcarine sulcus. This issue might be addressed using a more robust signal in terms of signal to noise ratio, either from the acquisition point of view using for instance a surface coil or from the signal processing aspect, averaging signals from multi-sessions recordings of the same subject. These technical and methodological issues shall be adressed in upcoming reports. Besides, the retinotopic areas segmentation is still not completely automatic, which could mainly raise the question of reproducibility of the ROIs derived for further analysis. We will therefore also explore more reliable techniques than the visual field sign computation we implemented, for instance warping a model on our maps as described in [5].

8 Appendix

A SPM batches

As mentioned in paragraph 4.2, we use SPM99 batches to specify our statistical model and the statistical tests to perform. Three files are needed:
- *do_stats.m*, which specify what SPM should do -in our case specify and estimate a model and estimate contrasts- and some paths and filenames of interest.
- *subs_model.m*, where the temporal filters to apply and the model regressors are defined. The functional images to load are also specified there.
- *subs_contrast*, where the contrasts to estimate are defined.

These batches are then read by SPM calling the command *spm_bch('do_stats')*. The 3 files for a given analysis are shown next. Parameters to tune are indicated with some comments. To understand further this batch system, you can refer to the code *spm_bch_man.m*.

a) do_stats.m

```
%---------------------------------
% user variables defined here
%---------------------------------
%---------------------------------
% batch variables defined here for analyses
%---------------------------------

analyses = struct( ...
   'type', [1 2], ...
   'index', [1 1], ...
   'work_dir', [1 1], ...
   'mfile', [1 2] ...
);

%----------------------

type = {'model','contrasts','defaults_edit','headers',...
   'means','realign','normalize','smooth'};

%----------------------

% work_dir = cellstr(sdirs);
work_dir = { ...
   '/results'...  %% PATH 1
   };

%----------------------

mfile = { ...
   '/matlab_tools/subs_model',...  %% PATH 2
   '/matlab_tools/subs_contrast'...  %% PATH 3
   };

%----------------------
```

b) subs_model.m

```
%--------------------------------
%--------------------------------
nb_slices_TR = X ; %% TO BE FILLED
TR = X ; %% TO BE FILLED
nb_scan_per_sess = X; %% NBR OF SCANS PER SESSION
nb_sess = 4;

fMRI_T = nb_slices_TR;
fMRI_T0 = 1;
sps = [];
hf_cut = [];
for sess = 1:nb_sess
   sps = [sps nb_scan_per_sess];
   hf_cut = [hf_cut X]; %% Stimulation Period in sec times 2.5
end

% %%%%%%%%%%%%%%%%%%%%%%%%%%%%%%%%%%%%%%%%%%%%%%%%%%%%%%%%%%%%%%%%%%%%%%%%%%%
F1 = spm_get('Files', '/fonc3','xretino*.img'); %% PATHS & NAMES
F2 = spm_get('Files', '/fonc4','xretino*.img'); %% TO SPECIFY
F3 = spm_get('Files', '/fonc5','xretino*.img');
F4 = spm_get('Files', '/fonc6','xretino*.img');

%--------------------------------
% batch variables defined here for analysis 'model'
%--------------------------------
% To define the model estimation parameters, refer to spm99/spm_fmri_spm_ui.m

model(1) = struct( ...
   'types', 4, ...  % Specify and estimate a model
   'global_effects', 'None', ...  % Global normalization
   'burst_mode', 0, ...  % 5472?
   'HF_fil', 'specify', ...  % High-pass filtering
   'HF_cut', hf_cut, ...  % Cutoff period (sec) (SOA_max*TR*2.5) for each session
   'LF_fil', 'Gaussian', ...  % Low-pass filtering
   'LF_cut', 4, ...  % case 'Gaussian'
   'int_corr', 'none', ...  % intrinsic autocorrelations (Vi)
   'now_later', 1, ...  %-Estimate now or later?
   'stop_writing', 1, ...  % Current directory contains existing SPMstats
                           % files 1-0 (stop - continue)
   'trial_fcon', 0, ...  % -Generate default trial-specific F-contrasts
```

```
                          % specified by session?
   % To define the model design, refer to spm99/spm_fMRI_design.m
   % and spm_get_ons.m
'RT', TR, ...  % 'Interscan interval secs'
'replicated', 0, ...  % are conditions replicated ?
'nsess', nb_sess, ...  % Nb of sessions
'nscans', sps, ...  % Nb of scans
'files', F1 F2 F3 F4, ...  % Functional scans for each sessions
'conditions_nb', [0 0 0 0], ...
'conditions', [0 0 0 0], ...
'regressors_nb', [2 2 2 2], ...  % get user specified regressors
'regressors', [1 2 3 4], ...
'parametrics_type', 'none','none','none','none', ...  % Parametric modulation
'parametrics', [], ...
'stochastics_flag', [0 0 0 0], ...  % stochastic designs
'stochastics', [] ...
);

A1 = cos(2*pi/18*(0:nb_scan_per_sess-1));
A2 = sin(2*pi/18*(0:nb_scan_per_sess-1));
db_reg = [A1;A2]';

regressors(1) = struct( ...
   'names', 'cos_ring_cont','sin_ring_cont', ...  %% REGRESSORS NAMES
   'values', db_reg ...  %ARRAY (num_scans x num_regressors)
);

regressors(2) = regressors(1);
regressors(2).names = 'cos_ring_exp','sin_ring_exp';

regressors(3) = regressors(1);
regressors(3).names = 'cos_wedge_clock','sin_wedge_clock';

regressors(4) = regressors(1);
regressors(4).names = 'cos_wedge_anti','sin_wedge_anti';

%-------------------------------- %--------------------------------
```

c) subs_contrast.m

```
%--------------------------------
% batch variables defined here for analysis 'contrasts'
%--------------------------------
%--------------------------------

%% F test for the 4 ring regressors (sessions 1 and 2)
con1 = [1 0 0 0 0 0 0 0 0 0 0 0];
con1 = [con1; [0 1 0 0 0 0 0 0 0 0 0 0]];
con1 = [con1; [0 0 1 0 0 0 0 0 0 0 0 0]];
con1 = [con1; [0 0 0 1 0 0 0 0 0 0 0 0]];

%% F test for the 4 wedge regressors (sessions 3 and 4)
con2 = [0 0 0 0 1 0 0 0 0 0 0 0];
con2 = [con2; [0 0 0 0 0 1 0 0 0 0 0 0]];
con2 = [con2; [0 0 0 0 0 0 1 0 0 0 0 0]];
con2 = [con2; [0 0 0 0 0 0 0 1 0 0 0 0]];

contrasts(1) = struct( ...
   'names', 'F(ring)', 'F(wedge)', ...  %% With respect to STIMULI ORDER
   'types', 'F', 'F', ...
   'values', con1,con2 ...
);
```

Contents

References

[1] L. M. Chalupa and J.S. Werner, editors. *The visual neurosciences*. MIT Press, 2004.

[2] Christophe Chefd'hotel, Gerardo Hermosillo, and Olivier Faugeras. Flows of Diffeomorphisms for Multimodal Image Registration. In *International Symposium on Biomedical Imaging*. IEEE, 2002.

[3] Y. Cointepas, J.-F. Mangin, Line Garnero, J.-B. Poline, and H. Benali. BrainVISA: Software platform for visualization and analysis of multi-modality brain data. In *Proc. 7th HBM*, page S98, Brighton, United Kingdom, 2001.

[4] E. DeYoe, G. Carman, P. Bandettini, S. Glickman, J. Wieser, R. Cox, D. Miller, and J. Neitz. Mapping striate and extrastriate visual areas in human cerebral cortex. *Neurobiology*, 93:2382-2386, March 1996.

[5] R. Dougherty, V. Koch, A. Brewer, B. Fischer, J. Modersitzki, and B. Wandell. Visual field representations and locations of visual areas v1/2/3 in human visual cortex. *Journal of Vision*, 3:586-598, October 2003.

[6] S. Dumoulin, R. Hoge, C. Baker, R. Hess, R. Achtman, and A. Evans. Automatic volumetric segmentation of human visual retinotopic cortex. *NeuroImage*, 18(3):576-587, 2003.

[7] S. Engel, D. Rumelhart, B. Wandell, A. Lee, G. Glober, E-J. Chichilnisky, and M. Shadlen. fmri of human visual cortex. *Nature*, 369:525-529, June 1994.

[8] L. Freire, A. Roche, and J.F. Mangin. What is the Best Similarity Measure for Motion Correction in fMRI Time Series? *IEEE Transactions on Medical Imaging*, 21(5):470-484, May 2002.

[9] K.J. Friston, J. Ashburner, et al. *SPM 97 course notes*. Wellcome Department of Cognitive Neurology, University College london, 1997.

[10] N. Hadjikhani, A. Liu, A. Dale, P. Cavanagh, and R. Tootell. Retinotopy and color sensitivity in human cortical area v8. *Nature Neuroscience*, 1(3):235-241, July 1998.

[11] E.R. Kandel, J.H. Schwartz, and T.M. Jessel. *Principles of Neural Science*. McGraw-Hill, 4th edition, 2000.

[12] J.J. Koenderink. The structure of images. *Biological Cybernetics*, 50:363-370, 1984.

[13] J-F. Mangin. Entropy minimization for automatic correction of intensity nonuniformity. In *IEEE MMBIA Workshop*, pages 162-169, Hilton Head Island, South Carolina, 2000. IEEE Press.

[14] J-F. Mangin, O. Coulon, and V. Frouin. Robust brain segmentation using histogram scale-space analysis and mathematical morphology. In W. M. Wells, A. Colchester, and S. Delp, editors, *Proc. 1st MICCAI*, LNCS-1496, pages 1230-1241, MIT, Boston, October 1998. Springer Verlag.

[15] S. Palmer. *Vision Science : Photons to Phenomenology.* MIT Press, 1999.

[16] W. Press, A. Brewer, R. Dougherty, A. Wade, and B. Wandell. Visual areas and spatial summation in human visual cortex. *Vision Research*, 41:1321-1332, 2001.

[17] M.I. Sereno, A.M. Dale, J.B. Reppas, K.K. Kwong, J.W. Belliveau, T.J. Brady, B.R. Rosen, and R.B.H. Tootell. Borders of multiple visual areas in human revealed by functional magnetic resonance imaging. *Science*, pages 889-893, 1995.

[18] M.I. Sereno, C.T. McDonald, and J.M. Allman. Analysis of retinotopic maps in extrastriate cortex. *Cerebral Cortex*, 4:601-620, 1994.

[19] S. Slotnick and S. Yantis. Efficient acquisition of human retinotopic maps. *Human Brain Mapping*, 18:22-29, 2003.

[20] A. Smith, M. Greenlee, K. Singh, F. Kramer, and J. Hennig. The processing of first- and second-order motion in human visual cortex assessed by functional resonance magnetic imaging (fmri). *The Journal of Neuroscience*, 18(10):3816-3830, May 1998.

[21] N. Sochen, R. Deriche, and L. Lopez-Perez. Variational beltrami flows over manifolds. In *International Conference on Image Processing*, 2003.

[22] R. Tootell, N. Hadjikhani, J. Mendola, S. Marrett, and A. Dale. From retinotopy to recognition: fmri in human visual cortex. *Trends in Cognitive Sciences*, 2(5):174-183, May 1998.

[23] R. Tootell, N. Hadjikhani, W. Vanduffel, A. Liu, J. Mendola, M. Sereno, and A. Dale. Functional analysis of primary visual cortex (v1) in humans. In *Proceedings of the National Academy of Sciences USA*, volume 95, pages 811-817, February 1998.

[24] R. Tootell, E. Switkes, M. Silverman, and S. Hamilton. Functional anatomy of the macaque striate cortex. ii. retinotopic organization. *Journal of neuroscience*, 8(5):1531-1568, 1988.

[25] R.B. Tootell and N. Hadjikhani. Where is 'dorsal v4' in human visual cortex? retinotopic, topographic and functional evidence. *Cerebral Cortex*, 11:298-311, April 2001.

[26] S. Van Oostende, S. Sunaert, P. Van Hecke, G. Marchal, and G. Orban. The kinetic occipital (ko) region in man: an fmri study. *Cerebral Cortex*, 7:690-701, 1997.

[27] A. Wade, A. Brewer, J. Rieger, and B. Wandell. Functional measurements of human ventral occipital cortex : retinotopy and colour. *Phil. Trans. R. Soc. Lond.*, 357:963-973, 2002.

[28] B. Wandell. Computational neuroimaging of human visual cortex. *Annual Review of Neuroscience*, 22:145-173, 1999.

[29] J. Warnking. *Delineation des aires visuelles retinotopiques chez l'homme par IRM fonctionnelle.* PhD thesis, Universite Joseph Fourier-Grenoble I, July 2002.

[30] J. Warnking, M. Dojat, A. Guerin-Dugue, C. Delon-Martin, S. Olympieff, N. Richard, A. Chehikian, and C. Segebarth. fmri retinotopic mapping - step by step. *NeuroImage*, 17:1665-1683, 2002.

[31] A.P. Witkin. Scale-space filtering. In *International Joint Conference on Artificial Intelligence*, pages 1019-1021, 1983.

[32] N. Wotawa, J-P. Pons, L. Lopez, R. Deriche, and O. Faugeras. fmri data smoothing constrained to the cortical surface: a comparison of the level-set and mesh-based approaches. In *NeuroImage (HBM'04)*, 2004.

[33] N. Wotawa, B. Thirion, E. Castet, J-L. Anton, and O. Faugeras. Efficient human retinotopic mapping using fMRI. In Tomas Paus, Ed Bullmore, and Jonathan D. Cohen, editors, *NeuroImage (HBM'03)*, New York, USA, 2003. Academic Press.

[34] S. Zeki. Improbable areas in the visual brain. *Trends in Neurosciences*, 26(1):23-26, January 2003.

Unité de recherche INRIA Sophia Antipolis
2004, route des Lucioles - BP 93 - 06902 Sophia Antipolis Cedex (France)

Unité de recherche INRIA Futurs : Parc Club Orsay Université - ZAC des Vignes
4, rue Jacques Monod - 91893 ORSAY Cedex (France)
Unité de recherche INRIA Lorraine : LORIA, Technopôle de Nancy-Brabois - Campus scientifique
615, rue du Jardin Botanique - BP 101 - 54602 Villers-lès-Nancy Cedex (France)
Unité de recherche INRIA Rennes : IRISA, Campus universitaire de Beaulieu - 35042 Rennes Cedex (France)
Unité de recherche INRIA Rhône-Alpes : 655, avenue de l'Europe - 38334 Montbonnot Saint-Ismier (France)
Unité de recherche INRIA Rocquencourt : Domaine de Voluceau - Rocquencourt - BP 105 - 78153 Le Chesnay Cedex (France)

Éditeur
INRIA - Domaine de Voluceau - Rocquencourt, BP 105 - 78153 Le Chesnay Cedex (France)
http://www.inria.fr
ISSN 0249-6399